A hybrid numerical model for simulating aero-elastic-hydro-mooring-wake dynamic responses of floating offshore wind turbine

Ziying Yu[a], Qingwei Ma[b], Xing Zheng[a], Kangping Liao[a], Binghan Sun[a], Abbas Khayyer[c]

[a]Harbin Engineering University, China
[b]City, University of London, UK
[c]Kyoto University, Japan

Abstract

It demands many computational resources to model the coupled responses of a floating offshore wind turbine (FOWT), especially for its aero-elastic-hydro-mooring-wake dynamics and their interaction. In this paper, a new hybrid numerical model for FOWT systems is developed, which is based on the hybrid potential-viscous flow model called qaleFOAM. In this model, the aerodynamics of wind turbine are solved by the unsteady actuator line method (UALM); the elastic responses of the turbine blade are calculated by the Legendre spectral finite element model (BeamDyn); the hydrodynamics of the floating platform are dealt with by the combination of the fully nonlinear potential solver and a two-phase Navier–Stokes solver; the mooring dynamics are considered with the Lumped Mass Mooring Model (MoorDyn), and the two-phase fluid dynamics in a region near the FOWT is solved by an finite volume method with the large eddy simulation (LES) modelling the turbulent effects. This newly formulated model can deal with wind, wave, mooring dynamics, platform motions, and turbine structural dynamics involved in the FOWT system. To demonstrate the capability of the present model, various cases with different complexities are investigated and compared with the experimental data and other numerical results. Then, the model is applied to simulation of a semi-submersible FOWT system, subjected to a regular wave and a uniform wind. The prediction of the aerodynamic performance, blade tip deflection, platform motion responses, and mooring line tension loads show good agreements with the results from other methods. In addition, the phenomenon of the coupled effects between the dynamic responses of platform, blade deformation and wake flow are captured reasonably well.

Keywords: floating offshore wind turbine; aero-elastic-hydro-mooring-wake dynamic responses; qaleFOAM; UALM; BeamDyn; MoorDyn; LES

1. Introduction

In recent year, the wind turbines are expanded to deep sea and large-scale with the development of technology and the demand of the energy (Hao et al., 2020). Floating offshore wind turbines (FOWTs) are sprouting, becoming more and more popular, and being expected to fast grow in the coming decades. The physics involved in the dynamic behaviors of a floating offshore wind turbine (FOWT) are quite complex. During harnessing wind energy, the turbine blade and tower vibrates, the vortexes are generated and the turbine thrust and torque oscillate, affecting the dynamic behavior of the floating platform. Besides, the wave loads acting on the floating platform and the mooring system cause the 6-DOF (six degrees of freedom) motions of the FOWT system. These motions will influence the wind turbine production, the turbine blade deformation, the mooring line tension and the wake flow field. A FOWT model should consider all the coupled physics and capture the aero-elastic-hydro-mooring-wake interaction accurately and efficiently.

One commonly used method is the high-fidelity approach. It is usually based on the Computational Fluid Dynamics (CFD) to directly solve the aero-hydro-wake dynamics. Meanwhile, the mooring system is simulated alone and added as

restraints to the floating body instead of directly calculated in the CFD computational domain. Tran and Kim (2016) adopted dynamic fluid-structure interaction method and overset technique in STAR-CCM+ to analyze the aero-hydro-mooring-wake dynamic and their interactions of a FOWT. Liu et al. (2017) created a multi sliding mesh handle the motion of the FOWT in regular wave and uniform wind in OpenFOAM. Zhou et al. (2021) improved the inflow wind condition to discuss the aerodynamic characteristic and platform motion prediction. However, such high-fidelity approach requires very high computational costs, sometime prohibitive. Therefore, researchers have tried to use models with different fidelities for different parts of problems. Li et al. (2015) coupled the multi-body dynamics (MBD) and CFD to study the explicit wind turbulence influence on the wake flow. Carrión et al. (2014) combined the Computational Structural Dynamics (CSD) and CFD to compare the static and dynamic response on the NREL (National Renewable Energy Laboratory) wind turbine. Moreover, Liu et al. (2019a, 2019b) developed the CFD-MBD method in OpenFOAM and establish the coupled aero-hydro-mooring-elastic tool in the FOWT system. Even so, these high-fidelity method with some simplification in some element still demands very high computational cost, especially for modeling FOWT arrays. One of reasons is because the wave fields for FOWT have to be considered, which are much larger in the scale than wind turbines themselves.

Another class of methods is simplified approach, or of low fidelity. In these methods, the load solver on the turbine blade is replaced by the Blade Element Momentum (BEM) theory, and the hydrodynamics are estimated by the Morison's equation or by linear wave potential theory. For structural dynamics, the blade is usually made equivalent to the beam model and solved with modal approach, MBD or Finite Element Method (FEM). Chen et al. (2019) combined them with the hybrid coordinate dynamic analysis method, quasi-static mooring modelling approach, a generator-torque controller and a full-span rotor-collective blade-pitch controller for simulating floating wind turbines. Ahn et al. (2020) used NREL's FAST code to simulate the aero–hydro–servo–elastic of a DTU 10 MW FOWT in the time domain. Jessen et al. (2019) compared the experimental, theoretical and FAST results of a scale model TLP FOWT. These simplified approaches have much less computational demand and are easily to be employed for analyzing fully coupled dynamic responses of a FOWT system. Nevertheless, they bear some limitations. For example, they ignore the nonlinear interaction between waves and platforms, which is essential for assessing and evaluating floating wind turbines.

A partly-simplified approach is also developed. The actuator line model (ALM) introduced by Sørensen and Shen (2002) is adopted to replace the influence of the turbine blade to the flow field, which is solved by CFD. It can significantly increase the computational efficiency compared to high-fidelity approach through avoiding use of the boundary layer grid around the blade surface and the sliding or overset mesh technique for blade rotation. Fleming et al. (2015) investigated the effect on the downstream wind turbine due to different yaw, tilt and position of the upstream turbine using such an approach. Duan et al. (2020) applied the approach in the wind farm simulation consist of 14 wind turbines and studied the wake flow interactions. Besides, Cheng et al. (2019) and Huang et al. (2019) analyzed the coupled aero-hydrodynamic of semi-submersible or spar type FOWT by unsteady ALM (UALM).

Another approach is to combine the fully nonlinear potential theory (FNPT) model with the N-S model based on the Navier–Stokes equations. In such an approach, the N-S models is employed within a small region near FOWT while the most part of wave field is handled by the FNPT model. This potential-viscous flow hybrid model can deal with the fully nonlinear interaction of FOWT with wave fields including very steep and breaking waves. The hybrid model can also efficiently reduce the size of the computational domain of N-S model and so increase the computational efficiency without sacrificing the accuracy caused by ignoring the nonlinear effects. The qaleFOAM is developed by the team of the authors based on this principle and by combining the quasi-arbitrary Lagrangian-Eulerian finite element method (QALE-FEM) for FNPT with the two-phase incompressible N-S solver called InterDyMFoam in OpenFOAM using the time/space splitting coupling (domain decomposition) strategy (Ma and Yan, 2006, 2009; Li et al., 2018; Yan et al., 2020). It has been evidenced that the qaleFOAM model can be several times faster than N-S models to achieve the similar level accuracy (Yan et al., 2020). In our previous publications, the aero-hydrodynamic analysis tool for FOWT modeling is established based on this model, and validated and verified for several cases (Yu et al., 2021, 2022). However, the turbine blades and tower are

treated as rigid and mooring lines are treated as quasi-static catenary lines in our previous work.

In this paper, the qaleFOAM will be further developed to make it not only able to deal efficiently with the fully nonlinear interaction between waves and platform but also take into account of structure dynamics of blades and mooring lines. In the newly-formed model, the wind turbine aerodynamics is solved by an improved unsteady ALM which is developed from traditional ALM code (Bachant et al., 2016); the blades structural dynamics is calculated by a Legendre spectral finite element code (BeamDyn) with geometrically exact beam theory (GEBT) (Wang et al., 2016), which is more accurate than the modal approach and easy to couple with ALM model than the MBD method. Mooring dynamics is considered through the Lumped Mass Mooring code (MoorDyn) described by Hall and Goupee (2015), which is expected to be more accurate than the original quasi-static catenary model (Bruinsma et al., 2018). By combing the qaleFOAM with BeamDyn and MoorDyn, the newly-formulated model, called qaleFOAM-BM hereafter for convenience can model the whole FOWT system with acceptable accuracy and efficiency. The capability of newly-developed qaleFOAM-BM will demonstrate by using it to simulate the NREL 5 MW OC4 semi-submersible floating offshore wind turbine (Jonkman et al., 2009; Coulling et al., 2013). The aerodynamic performance, blade tip elastic dynamics, platform motion responses, and mooring tension loads are validated with experimental and other numerical results from other publications, respectively. In addition, the cases with uniform wind and regular wave are investigated.

2. Methodology of qaleFOAM-BM

The present numerical model consists of 5 solvers as shown in Fig. 1. The QALE-FEM is adopted to solve the wave generation and propagation in a large domain (FNPT domain). The two-phase incompressible fluid flow (air and water) are solved by InterDyMFoam in OpenFOAM framework in the domain near the FOWT (N-S domain). The combination of these two parts is known as qaleFoam (Yan et al., 2020). The interaction between blade and aerodynamics is modelled by an improved unsteady ALM (UALM) with the actuator lines being flexible to confirm the deflection of blades. The blade structural dynamics is deal with by a Legendre spectral finite element (LSFE) method (BeamDyn) based on geometrically exact beam theory (GEBT). The mooring dynamics is handled by the lumped mass mooring method (MoorDyn).

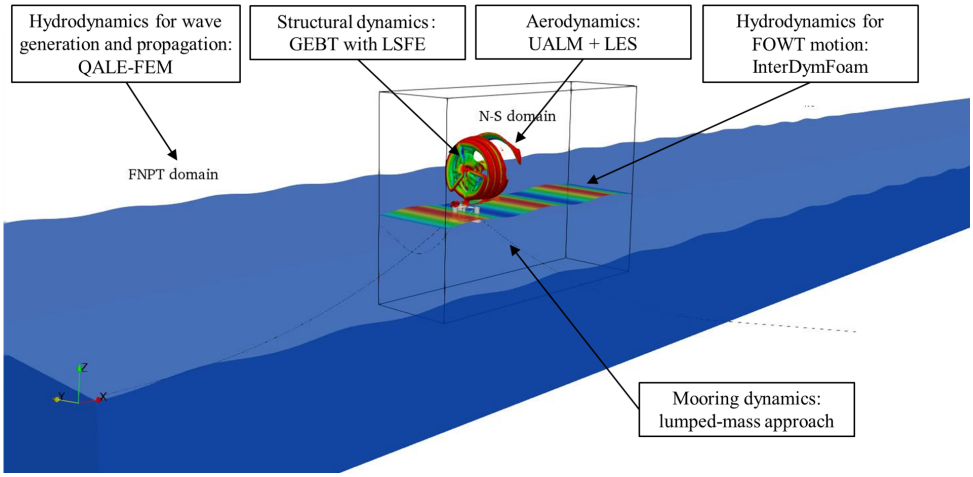

Fig. 1. Sketch of qaleFOAM-BM

2.1 Summary of qaleFOAM

The qaleFOAM without considering the blade and mooring dynamics has been proposed in our previous publications (Li et al., 2018; Yan et al., 2020; Yu, et al, 2022). A summary will be given below for completeness. This hybrid method was formulated by combing the full linear potential method (QALE-FEM) with the N-S model. In this method, the QALE-

FEM deal with the wave generation and propagation in the FNPT domain, assuming that the fluid is incompressible, inviscid and irrotational and described by velocity potential. The velocity potential Φ is governed by

$$\nabla^2\Phi = 0\,. \tag{1}$$

On the wavemaker, the velocity potential satisfies

$$\frac{\partial\Phi}{\partial n} = \boldsymbol{n}\cdot\boldsymbol{U} \tag{2}$$

in which U and n are the fluid velocity and normal vector of the wavemaker boundary.

On fixed boundaries such as the seabed

$$\frac{\partial\Phi}{\partial n} = 0 \tag{3}$$

On the free surface, both the kinematic and dynamic boundaries in a Lagrangian form are specified

$$\frac{D\boldsymbol{r}}{Dt} = \nabla\Phi \tag{4}$$

$$\frac{D\Phi}{Dt} = -gz + \frac{1}{2}|\nabla\Phi|^2 \tag{5}$$

where r is the position vector (x, y, z), and g is the gravitational acceleration with (x, y, z) being the right-hand coordinate system fixed on earth and $z = 0$ being on the mean free surface. In the FNPT domain, there is no structure.

The N-S method deals with the fluid flow including air and water near the structure with the volume of fluid (VOF) method capturing the free surface. To confirm to the motion of the structure, the arbitrary Lagrangian-Eulerian formulation is adopted. The governing equations for the model are

$$\frac{\partial\rho}{\partial t} + \nabla\cdot\rho\boldsymbol{U} = 0 \tag{6}$$

$$\frac{\partial\rho\boldsymbol{U}}{\partial t} + \nabla\cdot[\rho(\boldsymbol{U}-\boldsymbol{U}_g)\boldsymbol{U}] = -\nabla p - \rho\boldsymbol{g} + \nabla\cdot(\mu\nabla\boldsymbol{U}) + \nabla\boldsymbol{U}\cdot\nabla\mu + \rho\boldsymbol{f}_{UALM} \tag{7}$$

$$\frac{\partial\alpha}{\partial t} + \nabla\cdot\alpha(\boldsymbol{U}-\boldsymbol{U}_g) + \nabla\cdot\boldsymbol{U}_c\alpha(1-\alpha) = 0 \tag{8}$$

where ρ is the fluid density; $\boldsymbol{U}_g$ is the computational grid velocity; p is the dynamic pressure; $\boldsymbol{g}$ is the vector of the gravitational acceleration; μ is the dynamic viscosity; $\boldsymbol{f}_{UALM}$ is the source item to model the blade effects on the fluids; $\boldsymbol{U}_c$=min$\{c_a|\boldsymbol{U}|,$ max $(|\boldsymbol{U}|)\}$ is the relative compression velocity; and α is the volume fraction which $\alpha = 0$ and $\alpha = 1$ represent the air phase and water phase, respectively. The density and the viscosity of the fluid are expressed by

$$\rho = \rho_{air}(1-\alpha) + \rho_{water}\alpha \text{ and } \mu = \mu_{air}(1-\alpha) + \mu_{water}\alpha \tag{9}$$

with the subscripts 'air' and 'water' denoting the quantities for air and water, respectively.

These two models are coupled by zonal approach illustrated in Fig. 1. Wave is generated by the wavemaker far away from the floating object based on the second order wavemaker theory (Yan et al., 2015, Yan et al 2020). The generated wave is transited into the N-S domain through the relaxation zone technique at the inlet (submerged) boundary of the N-S domain. In the relaxation zone, the physical quantities for the N-S solver, velocity u, pressure p and wave elevation η, are corrected by.

$$f(x,y,z) = f_{NS}(x,y,z)w + f_{FNPT}(x,y,z)(1-w) \tag{10}$$

where w is the weighting function, which is 0 on the inlet boundary of N-S domain and gradually increase to 1 on the other boundary of the relaxation zone; the subscripts NS and FNPT represent the quantities from the N-S solver or QALE-FEM.

It is noted that the QALE-FEM is a single-phase model, only dealing with the water phase. To smoothly couple the single-phase and two-phase model, the velocity on the coupling boundary near the free surface are corrected by

$$\boldsymbol{u}(x,y,z) = \begin{cases} \nabla\Phi(x,y,z) & z \le \eta \\ (1-R_z)\nabla\Phi(x,y,\eta) + R_z\boldsymbol{u}_w(x,y,z) & z > \eta \end{cases} \tag{11}$$

where, $\boldsymbol{u}_w$ is the wind speed; and R_z is the weighting function varying from 0 to 1; and η is the elevation of interface between air and water. As shown in Eq. (11), the fluid velocity above the free surface is defined by a weighted summation of the corresponding water velocity on the free surface and the wind velocity to smooth transition of the fluid velocity from the water phase to the air phase. For other details about qaleFOAM, readers are suggested to see the references mentioned about.

2.2 Interaction between aerodynamics and blades

Traditional actuator line method has been used by many researchers to replaces the true blade by a actuator line to model the interaction between blades and aerodynamics. This method does not take into account of the effects of the platform motions and blade deflection. It has been demonstrated that it works well for a fixed wind turbine with rigid turbines in our previous research (Yu et al., 2018a, 2018b, 2020). Taking account into the FOWT motion, it needs to be extended into the unsteady actuator line model (Cheng et al., 2019). In their model, they considered the effects of the displacement and velocities of floating system on the location of each actuator element and relative velocity of actuator element. However, they considered the blades as rigid, i.e., ignoring effects of blade deflections, which can be important for large wind turbines.

In this paper, the unsteady actuator line model is improved to take into account of both FOWT motions and blades' defection. The actuator line of each blade is located at the aerodynamic center, about 0.25 local chord length. As illustrated in Fig. 2, the relative velocity $\boldsymbol{U}_{rel}$ of an actuator element is described by

$$\boldsymbol{U}_{rel} = \boldsymbol{U}_{in} + \boldsymbol{\Omega} \times \boldsymbol{r} - \boldsymbol{U}_{rot} + \boldsymbol{U}_{M} + \boldsymbol{U}_{def} \tag{12}$$

where $\boldsymbol{U}_{in}$ is the component of the inflow velocity normal to the rotor plane while $\boldsymbol{U}_{rot}$ is the component of the inflow velocity in the rotor plane; $\boldsymbol{\Omega}$ is the rotate angular velocity of the turbine; $\boldsymbol{r}$ is the distance from the rotating axis of the turbine to the actuator element; $\boldsymbol{U}_M$ is the resulting velocity caused by the motions of the FOWT platform subjected to waves; $\boldsymbol{U}_{def}$ is the velocity caused by the blade deflection.

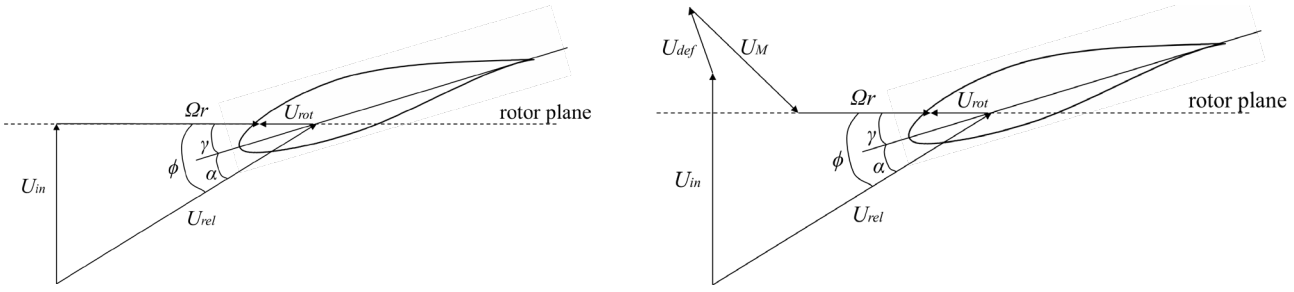

(a) (b)

Fig. 2. Sketch of the relative velocity calculation in the blade elements: (a) traditional actuator line method; (b) improved unsteady actuator line method. ϕ is the angle between the relative velocity and the rotor plane; γ is the twist angle and α is the attack angle.

The aerodynamic loads $\boldsymbol{f}_{aero}$ of each actuator element can be estimated by,

$$\boldsymbol{f}_{aero} = (\boldsymbol{L}, \boldsymbol{D}) = \frac{1}{2} \rho_{air} A_{elem} \, | \boldsymbol{U}_{rel} |^2 \, (C_l \boldsymbol{e}_L + C_d \boldsymbol{e}_D) \tag{13}$$

where, $\boldsymbol{L}$ and $\boldsymbol{D}$ are the lift and drag, respectively; ρ_{air} is the air density; c is the local chord length of the airfoil; A_{elem} is the blade element planform area equal to $c \times \Delta l$ with c being local chord length and Δl the length of an actuator element; C_l and C_d are the lift and drag coefficient, respectively. They are determined by the 2D airfoil data and corrected by the 3D effects (Sørensen and Shen, 2002); $\boldsymbol{e}_L$ and $\boldsymbol{e}_D$ are the unit vector in lift and drag direction.

In addition, the circulation of the rotor near the blade tip should tend to 0 according to Shen et al. (2005). The Prandtl-Glauert tip loss model is used in this paper. Then the actuator element loading should be corrected by

$$F_{tip} = \frac{2}{\pi}\arccos[\exp(-\frac{B(R-r)}{2r\sin\phi})] \tag{14}$$

where, F_{tip} is the tip loss coefficient; B is the number of the blades and R is the radius of the turbine.

Eq. (13) represented the force acting on turbine blades, reflecting the effects of aerodynamics on blade dynamics. On the other hand, the forces acting on fluids due to blades, or in other words the effects of blades on the aerodynamics, should be equal to that given in Eq. (13) in magnitude but in opposite direction. Nevertheless, it should be distributed in the air domain rather than just applied on the actuator line. The distributed force is estimated by

$$\eta_\varepsilon(d) = \frac{1}{\varepsilon^3\pi^{3/2}}\exp[-(\frac{d}{\varepsilon})^2] \tag{15}$$

$$\boldsymbol{f}_{UALM} = -F_{tip}\boldsymbol{f}_{aero} \otimes \eta_\varepsilon(d) \tag{16}$$

where d is the distance from the aerodynamic center to a point in the air domain, and ε is a parameter that control the distribute range. According to Shives et al. (2012) and Bachant et al. (2016), ε is set as 4 times of the minimum local grid size here in the air domain. It is noted here that the aerodynamic center moves with time caused by the rotation of the turbine, motion of floating platform and dynamic deflection of blades.

Except for the blades, the interaction of hub and tower of the wind turbine with the aerodynamics is also modelled by the UALM. However, the airfoils are changed into cylinders for these two parts. The relative velocities of these two parts are estimated by considering the motion of the FOWT system but not structural deflection (see Eq. (12)). This means that the tower and hub is rigid in the present study, which will be improved in future work. Others are similar to Eq. (13), Eq. (15) and Eq. (16) but tip loss coefficient is not applied. It should be noted that the dynamic stall effects (Leishman et al., 1989) are not considered here, unless mentioned otherwise, which is acceptable for most of the cases considered in this paper.

2.3 Structural dynamics of blades

The structural dynamics of the wind turbine blades is described by geometrically exact beam theory (GEBT) (Reissner, 1973) and solved by using the Legendre spectral finite element (BeamDyn). The details were given by Wang et al. (2016) but the summary will be given below.

For each beam element, there are 6-DOF including the three translation and three rotation components as shown in Fig 3, governed by

$$\frac{\partial \boldsymbol{h}_e}{\partial t} - \frac{d\boldsymbol{F}_s}{d\boldsymbol{s}} = \boldsymbol{f}_s \tag{17}$$

$$\frac{\partial \boldsymbol{g}_e}{\partial t} + \frac{\partial \tilde{\boldsymbol{u}}}{\partial t}h_e - \frac{d\boldsymbol{M}_s}{d\boldsymbol{s}} - (\tilde{\boldsymbol{x}}_0 + \frac{\partial \tilde{\boldsymbol{u}}}{\partial \boldsymbol{s}})\boldsymbol{F}_s = \boldsymbol{m}_s \tag{18}$$

where, $\boldsymbol{h}_e$ and $\boldsymbol{g}_e$ are the linear and angular momenta of the beam element, respectively; $\boldsymbol{F}_s$ and $\boldsymbol{M}_s$ are the internal force and moment for the beam section, respectively; $\boldsymbol{u}$ is the displacement before deformation; $\boldsymbol{x}_0$ is the initial position vector; $\boldsymbol{f}_s$ and $\boldsymbol{m}_s$ are the external distributed force and moment for the beam element, respectively. They are obtained by transforming the aerodynamic loads $\boldsymbol{f}_{aero}$, and detailed process can refer to Section 2.6. The superscript '~' is defined as the corresponding skew-symmetric tensor, and as shown in Eq. (19).

$$\tilde{\boldsymbol{f}} = \begin{bmatrix} 0 & -f_z & f_y \\ f_z & 0 & -f_x \\ -f_y & f_x & 0 \end{bmatrix} \tag{19}$$

where $\boldsymbol{f}$ is the variables (such as $\boldsymbol{u}$ or $\boldsymbol{x}_0$) concerned.

The relationships of the velocities and the momenta, the strain measures and the sectional resultants can be described as,

$$\begin{Bmatrix} \boldsymbol{h}_e \\ \boldsymbol{g}_e \end{Bmatrix} = [M_e] \begin{Bmatrix} \boldsymbol{v}_e \\ \boldsymbol{w}_e \end{Bmatrix} \tag{20}$$

$$\begin{Bmatrix} \boldsymbol{F}_s \\ \boldsymbol{M}_s \end{Bmatrix} = [K_e] \begin{Bmatrix} \boldsymbol{\varepsilon}_e \\ \boldsymbol{\kappa}_e \end{Bmatrix} \tag{21}$$

in which, $[M_e]$ and $[K_e]$ are the sectional mass and stiffness matrices, respectively; $\boldsymbol{\varepsilon}_e$ and $\boldsymbol{\kappa}_e$ are the strains and curvatures, respectively; $\boldsymbol{v}_e$ and $\boldsymbol{w}_e$ are the linear and angular velocity of the beam element, respectively.

The governing equations of a whole blade are obtained by integrating all beam elements according to the trapezoidal method, and then solved by Newton-Raphson method. The LSFE method is used to discretize it into several Gauss-lobatto-Legendre points. The time integration adopts the generalized-α scheme with second-order accuracy. Besides, a linearization process is applied to deal with the nonlinearity in the original governing equations. The linearized discretized governing equations for Eq. (17) and Eq. (18) can be written as,

$$[\bar{M}_e]\Delta\bar{\boldsymbol{a}}_e + [\bar{G}_e]\Delta\bar{\boldsymbol{v}}_e + [\bar{K}_e]\Delta\bar{\boldsymbol{q}}_e = \bar{\boldsymbol{F}}_{e0} - \bar{\boldsymbol{F}}_e \tag{22}$$

where, $\boldsymbol{a}_e$, $\boldsymbol{v}_e$ and $\boldsymbol{q}_e$ are the displacement, velocity and acceleration of the element; $[G_e]$ is the gyroscopic matrices; $\boldsymbol{F}_{e0}$ is the external loads; $\boldsymbol{F}_e$ is the elemental forces. The superscript '-' is the linearized form of each term. More details can refer to Wang et al. (2016).

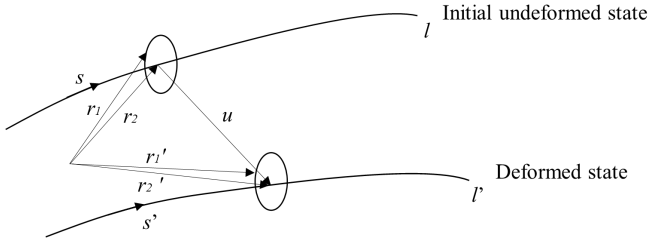

Fig. 3. Sketch of the deformed blade state

2.4 Mooring dynamics

To solve the mooring dynamics, a dynamic model, MoorDyn (Hall and Goupee, 2015), is employed here. This model considers the axial elasticity, hydrodynamic loading estimated by Morison's equation, and bottom contact. The mooring lines is split into a number of elements with the same length. The lumped-mass approach is adopted to discretize the dynamic equations of the mooring lines. The weight of each element is lumped at a corresponding node as shown in Fig. 4. The dynamics of each node satisfy,

$$[\boldsymbol{m}_i + \boldsymbol{a}_{pi} + \boldsymbol{a}_{qi}]\frac{\partial^2 \boldsymbol{r}_i}{\partial t^2} = \boldsymbol{T}_i + \boldsymbol{C}_i + \boldsymbol{W}_i + \boldsymbol{B}_i + \boldsymbol{D}_{pi} + \boldsymbol{D}_{qi} \tag{23}$$

where, subscript i means node i; $\boldsymbol{a}_p$ and $\boldsymbol{a}_q$ are the added mass in the transverse and tangential direction; $\boldsymbol{m}_i$ is the mass matrix of node i; $\boldsymbol{T}_i$ is the tension in cable, and it contains the tension by the adjacent nodes $\boldsymbol{T}_{i+1/2}$ and $\boldsymbol{T}_{i-1/2}$. $\boldsymbol{C}_i$ is the internal damping force, and also provided by the adjacent nodes $\boldsymbol{C}_{i+1/2}$ and $\boldsymbol{C}_{i-1/2}$; $\boldsymbol{W}_i$ is the net buoyancy of node i and calculated by the gravity and buoyance; $\boldsymbol{B}_i$ is the force when the node contacts the seabed; $\boldsymbol{D}_{pi}$ and $\boldsymbol{D}_{qi}$ are the transverse and tangential drag force, respectively. At the end nodes connected to the fairleads of the platform, the tension $\boldsymbol{T}_i$ becomes $\boldsymbol{T}_{Moor}$ which is

added as the external force into the equations of floating body dynamics (see Eq. (24)), and $\boldsymbol{r}_i$ and $\frac{\partial \boldsymbol{r}_i}{\partial t}$ in Eq (23) are equal to the displacement and velocity of the fairleads, which will be evaluated by Eq. (24) below. More details about Moordyn can be referred to Hall and Goupee (2015).

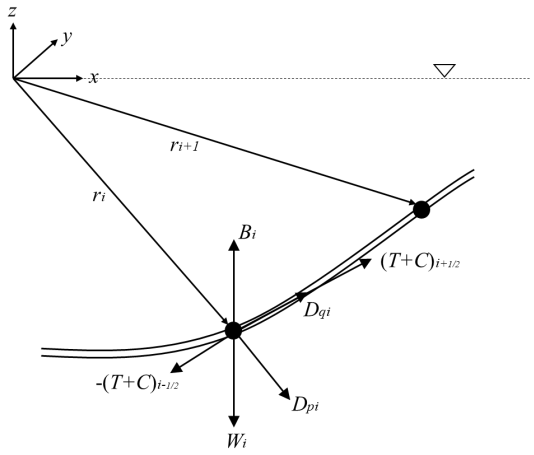

Fig. 4. Sketch of forces exerted on node *i* in the mooring line

2.5 Floating body dynamics

In the N-S domain, the 6-DOF motions of the floating bodies are calculated by Newton's 2nd law. However, the rotation is described by the Euler angles θ in qaleFoam instead of the orientation tensor Q in OpenFOAM.

$$[M]\dot{\boldsymbol{V}} = \boldsymbol{F}_{Hydro} + \boldsymbol{F}_{Aero} + \boldsymbol{T}_{Moor} \tag{24}$$

$$[I]\dot{\boldsymbol{w}} + \boldsymbol{w} \times [I]\boldsymbol{w} = \boldsymbol{M}_{Hydro} + \boldsymbol{M}_{Aero} + \boldsymbol{M}_{Moor} \tag{25}$$

$$\frac{d\boldsymbol{S}}{dt} = \boldsymbol{V} \tag{26}$$

$$[B]\frac{d\boldsymbol{\theta}}{dt} = \boldsymbol{w} \tag{27}$$

where $[M]$ and $[N]$ are the mass and inertia-moment matrix of the floating body; $\boldsymbol{S}$, $\boldsymbol{V}$ and $\dot{\boldsymbol{V}}$ are the translational displacement, velocity and acceleration, respectively; $\boldsymbol{F}$ and $\boldsymbol{M}$ are the external forces and moment acting on the platform. The subscript *Hydro* represents the forces solved by the qaleFoam, which is estimated by integrating all pressure and shear stresses over the floating platform surface. The subscript *Aero* means the force and moment evaluated by the improved unsteady ALM, Eq. (13), which includes the total loads on blades, hub and tower, expressed by $\boldsymbol{F}_{Aero} = \sum F_{tip}\boldsymbol{f}_{aero} + \sum \boldsymbol{f}_{towerAndHub}$ and $\boldsymbol{M}_{Aero} = \sum \boldsymbol{r}_b \times F_{tip}\boldsymbol{f}_{aero} + \sum \boldsymbol{r}_t \times \boldsymbol{f}_{towerAndHub}$, where $\boldsymbol{r}_b$ is the vector from the aerodynamic center of each blade actuator element to the FOWT mass center, and $\boldsymbol{r}_t$ is the vector from the tower or hub actuator element to the FOWT mass center. $\boldsymbol{M}_{Moor}$ can also be expressed by $\boldsymbol{M}_{Moor} = \boldsymbol{r}_m \times \boldsymbol{T}_{Moor}$, in which $\boldsymbol{r}_m$ is the vector from the fairleads position to the FOWT mass center. $\boldsymbol{w}$ and $\dot{\boldsymbol{w}}$ are angular velocity and acceleration and $[B]$ is the transformation tensor which is consist of the Euler angles θ (α, β, γ), expressed by

$$[B]=\begin{bmatrix}\cos\beta\cos\gamma & \sin\gamma & 0\\ -\cos\beta\sin\gamma & \cos\gamma & 0\\ \sin\beta & 0 & 1\end{bmatrix} \tag{28}$$

2.6 Fully coupled model

Main contribution of this paper is to couple all the models together to form one for simulating the whole FOWT system. In this section, some details will be discussed about the coupling. The coupling process is illustrated in Fig. 5. When the simulation starts, the flow field and all models are initialized firstly. During the certain period from start, only the QALE-FEM model in the FNPT domain is solved to generate and propagate the wave. This stage continues until the wave arrives at the inlet of the N-S domain. That is because the wave does not affect the structure before this time. After this time, all models start to run. In each new time step after that, the forces and moment on the platform will be estimated using the information available in previous steps, which include the thrust and torque from turbine, loads from the tower and hub, the tension at the fairleads of mooring lines and wave loadings on the platform. On this basis, the floating body dynamic equations will be solved to give the motions (displacement and velocity) of the platform. The results will be used to update the relative velocity of each the blade (i.e., actuator lines), their attack angles as well as the aerodynamic loads on them. The aerodynamic loads will be transferred to the equations of structural dynamics in one hand. On the other hand the aerodynamic loads will also be distributed into the fluid domain. After this, the solvers for structure dynamics, mooring dynamics and fluid dynamics will be run separately. The solutions obtained will be used for updating in the next time step. It is noted that the time step required for solving the blade structure dynamics is commonly less than that for solving fluid dynamics. One may use the smaller time step but the computational cost for solving the fluid dynamics would be much higher if doing so. To avoid the problem, sub-time steps in the structural solvers is applied for each time step of the fluid solver. For the cases considered in this paper, 5 sub-steps are performed on the structural solvers for each time step of the fluid solver. More details about coupling are discussed in the following paragraphs.

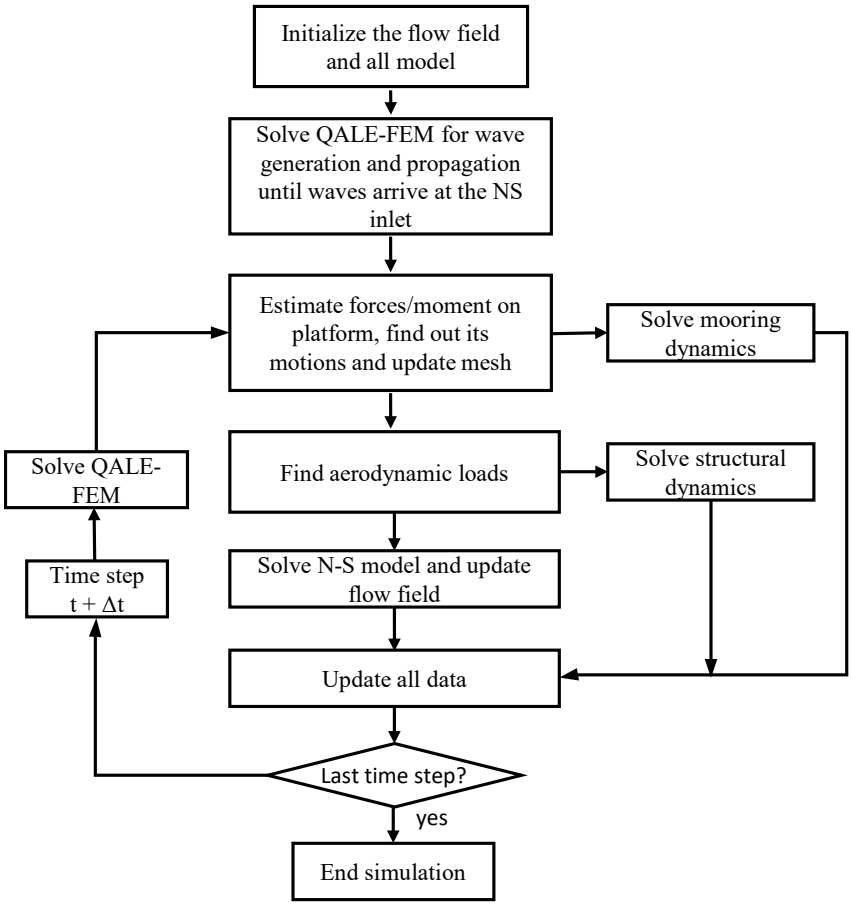

Fig. 5. Flow chart of the floating offshore wind turbine fully coupled model

(A) Coupling between aerodynamics and floating body dynamics

The effects of aerodynamics on the floating body dynamics are reflected by the thrust and torque of the turbine and forces on the tower and hub which are estimated using the ALM as described above. The effects of floating body dynamics on the turbine and its tower are the reflected by involving the velocities ($\boldsymbol{U}_M$) in Eq. (12) and by considering the displacement due to the floating body motions in determining the position of actuator elements.

Besides, the floating body motion can cause the significant deformation of the grids around it. If the dynamic mesh technique is used directly, the grid near the tower and turbine blades may also vary. This will lead to additional computational costs and downgrade the accuracy. The more computational costs are due to squeezing the grids near the structures and so reducing the time step. The negative effect on the accuracy is attributed to the deformed grids affecting the accuracy of interpolation involved in the ALM. To overcome the problems, a multizone moving mesh approach (Yu et al., 2021, 2022) is adopted. In this approach, the grids in Zone B move together as a whole with the floating platform. Zone B, as shown in Fig. 6, covers the turbine, bub, tower and platform. Outside Zone B, the dynamic mesh technique is employed. Using this approach, the grid deformation near the turbine and tower caused by the platform motion is eliminated.

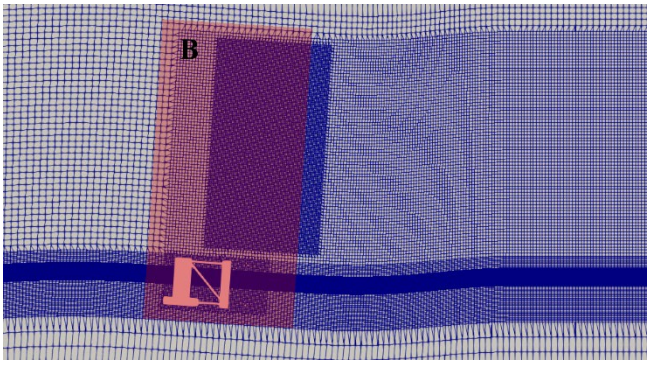

Fig. 6. Sketch of the multizone moving mesh technique for FOWT motion

(B) Coupling between aerodynamics and structural dynamics (BeamDyn)

The aerodynamic solver provides the loads for the blade structural dynamic solver (BeamDyn), which is estimated by Eq. (13). On other hand, the structural dynamic solver feedback the position and velocity of actuator elements which will be used in Eq. (12), (15) and (16). It is noted that the size of actuator elements are usually different from these of the structural elements. Due to this, if the force calculated by Eq. (13) is directly interpolated onto the structural elements, the resulting forces on the structure will be different from that of the forces acting on the fluid by the structure. This can be avoided by dividing the length of the actuator element before the interpolation is performed. After the interpolation, the point force on the structural elements are obtained by multiplying the length of structural elements. In addition, the points on the structure and their relations with the grid points of fluid dynamics solver continuously change with time due to turbine rotation, platform motions and blade deflection. That means that we need to find out the group of fluid grids which are linked to the specific structure point concerned every time step. This is potentially costing for the cases with a larger number of fluid domain grids. Thanks to the multizone technique employed as discussed for Fig. 6, it is possible for us to search only these fluid grid points within Zone B because all the structural points will be within this zone. This makes searching much more efficient than that for searching the whole fluid domain.

(C) Coupling between mooring dynamics and floating dynamics

The FOWT motions change the position of the fairleads of the mooring lines, and so their configuration. The displacements and velocities of the platform motions need to be transferred to the mooring dynamics solver (MoorDyn). The tensions of mooting lines at the fairleads affects the motions of the platform as shown in Eq. (24) and Eq. (25). These need to be transferred to the floating body dynamic solver. The exchanges of the data between the solvers are quite straightforward, thanks to the fact that the MoorDyn takes and outputs the required data in the same coordinate as that of the floating body dynamic solver. It is noted that the time step for the solvers can be different but they are the same in the work of this paper. More examination on this aspect will be carried out in future work.

3 FOWT model for simulation

The newly developed model is to apply to simulate the NREL 5 MW OC4 semi-submersible floating offshore wind turbine in order to demonstrate its capability and accuracy. The geometry parameters, air foil data, structural properties can be referred to the NREL reports (Jonkman et al., 2009). The properties and data from the reference are briefly summarized in Table. 1. The NREL 5 MW wind turbine is a three-blade, upwind, horizontal axis turbine and its blade has 61.5 m length. The three blades are fixed around the hub and installed on the top of the tower. The tower is attached to the main column of the OC4 semi-submersible floating platform. This floating platform has three offset columns for buoyancy and a series of smaller cross braces for strengthen the structure. Besides, the platform is moored by three catenary lines and the distribution of the mooring system is illustrated in Fig 7.

Table. 1. NREL 5 MW OC4 semi-submersible floating offshore wind turbine properties

Properties	Value
Turbine rotor diameter (m)	126
Hub diameter (m)	3
Hub height (m)	90
Shaft tilt angle (deg)	5
Rated wind speed (m/s)	11.4
Rated rotor speed (rpm)	12.1
Rated power (MW)	5.0
Platform mass (kg)	13,444,000
Draft (m)	20
Centre of mass below waterline (m)	9.9376
Total roll inertia (kg m2)	1.1×10^{10}
Total pitch inertia (kg m2)	1.1×10^{10}
Total yaw inertia (kg m2)	1.226×10^{10}
Equivalent Mooring Line Mass Density (kg/m)	113.35
Unstretched mooring line length (m)	835.5
Mooring Line Diameter (m)	0.0766
Equivalent mooring line extensional stiffness (N)	7.536×10^{8}
Transverse drag coefficient for mooring line	2.0
Tangential drag coefficient for mooring line	0.4
Transverse added mass coefficient for mooring line	0.8
Tangential added mass coefficient for mooring line	0.25

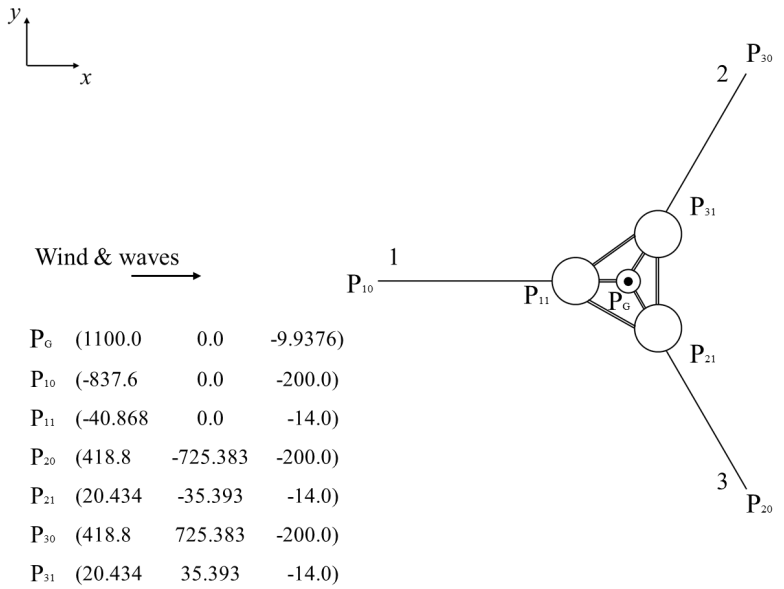

Fig. 7. Distribution of the OC4-DeepCWind semi-submersible platform mooring system and coordinates of the key points shown in drawing

The whole simulation domain is illustrated in Fig. 8. The length of FNPT domain is set as 6000 m, and the distance from the QALE-FEM wavemaker to inlet of the N-S domain is 950 m. The N-S domain is a rectangular zone with the size

of 650 m (x) × 200 m (y) × 460 m (z). The inlet and outlet boundaries are 150 m (about 1D of the turbine rotor) and 500 m (about 4D of the turbine rotor) away from the center of the platform. The water depth is 200 m. The incident wave studied in this paper has a wave height of 7.58 m and wave period of 12.1 s. The time step is set to 0.025 s corresponding to the blade rotates about 2 degrees in the uniform wind speed of 11.4 m/s and platform moves about 1/484 wave period. On this basis, structural solver run 5 cycles for each time step. As is shown in the Fig. 8, the turbine blade, hub and tower are replaced by corresponding actuator lines.

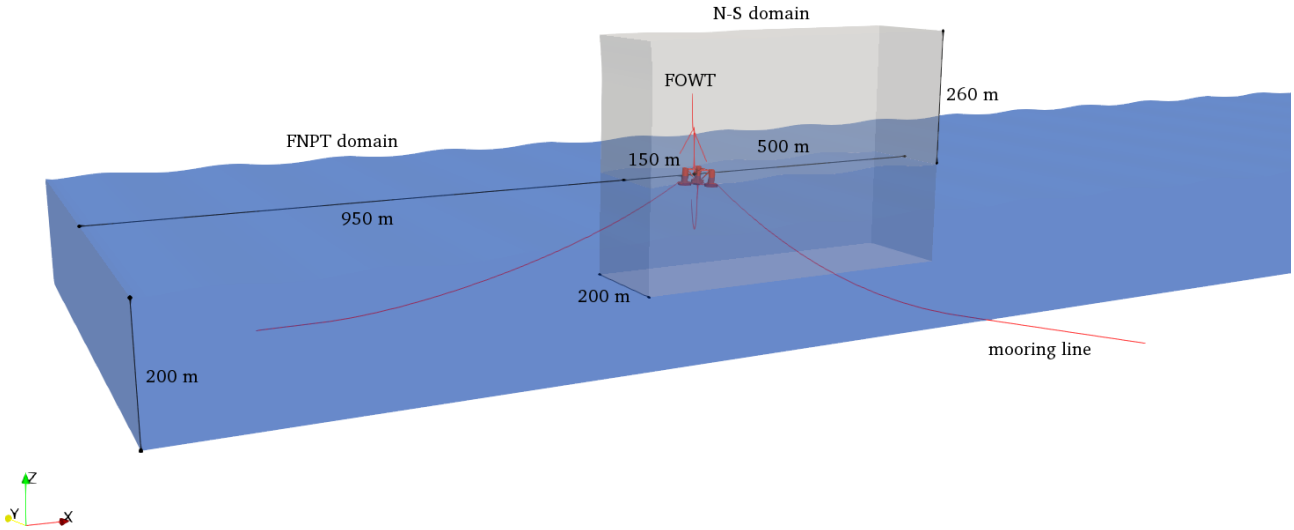

Fig. 8. Sketch of the whole domain with NREL 5 MW OC4 semi-submersible FOWT system

The computational mesh in the N-S domain is generated by the blockMesh - topoSet + refineMesh - snappyHexMesh utility in OpenFOAM and illustrated in Fig 9. The size of the background mesh is 4 m and refined 2 times. Therefore, the mesh near wind turbine is 1 m. Meanwhile, the refined grid size of 2 m is extended to the outlet of the N-S domain in order to study the far wake field. The horizontal grid size near free surface is set as 2 m corresponding to nearly 1/114 wave length. The vertical grid size near the free surface is set as 1/3 m corresponding to nearly 1/23 wave height. Therefore, the total number of cells is almost 5.28 million. The selection of the grid size and time step are based on our previous convergent tests (Yu et al., 2018b, 2020, 2022). In addition, the pressure-velocity coupling is solved with a combination algorithm called PIMPLE (Pressure Implicit with Splitting of Operator (PISO) and Semi-Implicit Method for Pressure-Linked Equations (SIMPLE)). The Large Eddy Simulation (LES) with WALE (Wall-Adapting Local Eddy-viscosity) model is considered in this paper. More details about the PIMPLE algorithm and the turbulence model equations could be referenced form the documents and codes in OpenFAOM 5.x.

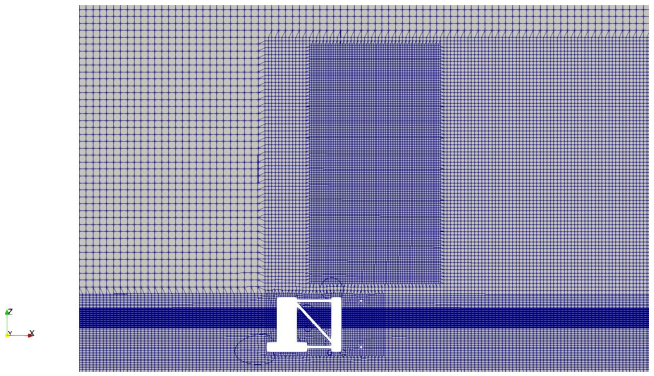

Fig. 9. Computational grid for the N-S domain

4. Validation

The newly developed model is validated in several aspects, which will be discussed in the next sub-sections. To use the existing results in public domain for this purpose, different situations are considered. The cases for the validation are defined in Table 2. These cases span from blade only, turbine with tower to platform with mooring lines.

Table. 2. Definition of the cases for validation (×: this aspect not considered)

Case No.	Wind turbine motion	Blade number	Blade motion	Tower	Blade deflection	Platform	Wind speed	Wave
Case 1	Fixed	3	Rotation	×	√	×	7~11.4	×
Case 2	Given Surge	3	Rotation	×	√	×	11.4	×
Case 3	×	1	Fixed	×	×	×	0	×
Case 4	×	1	Rotation	×	×	×	0	×
Case 5	×	0	×	×	×	√	0	×
Case 6	×	0	×	×	×	√	0	√

4.1 Aerodynamics of the wind turbine

The power and thrust of the fixed wind turbine defined in Case 1 are examined first. The rotor speed corresponding to different wind speed can refer to Jonkman et al. (2009). The present results for different wind speeds are compared with other results, including the prediction from FAST (Jonkman et al., 2009), the results obtained by using STAR-CCM+ (Wang et al., 2020), and our previous results by physical blade model (not ALM used) (Yu et al., 2021, 2022). As shown in Fig. 10, the results given by the newly developed method is in good agreement with the results from cited publications, especially for the power. It can be seen from the relative errors with FAST results in Table 3 that the maximum difference is less than 7.5 %, which certifies the reliable level of present model in aerodynamics.

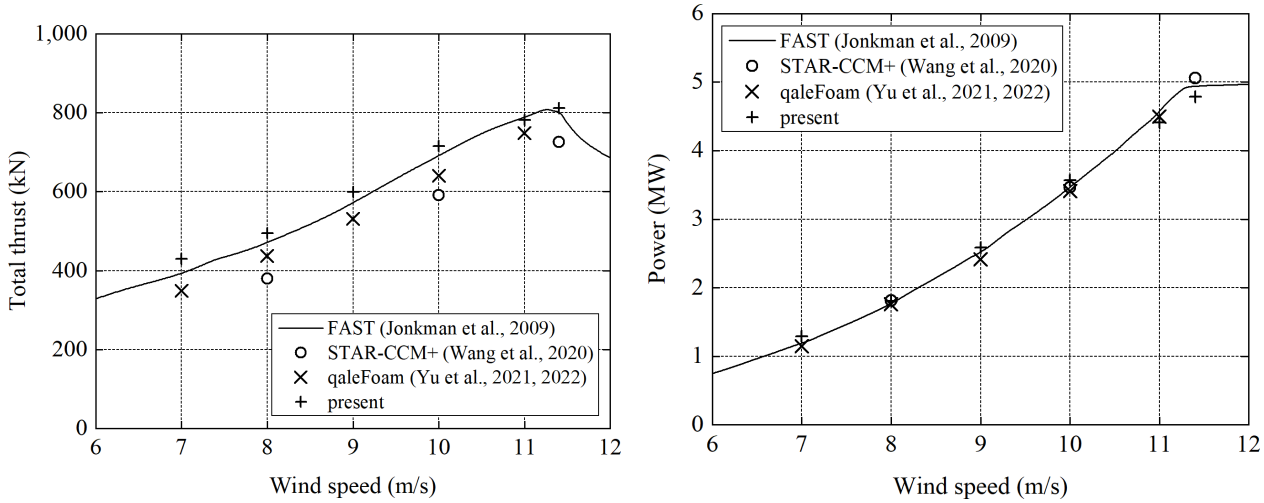

(a) (b)

Fig. 10. Comparisons with different numerical results in literature for Case 1: (a) total thrust; (b) power

Table. 3. Relative differences of the aerodynamics with FAST results (Case 1)

Wind speed (m/s)	Thrust	Power
8.0	7.47%	0.33%
9.0	4.68%	1.62%

10.0	4.61%	0.19%
11.0	1.42%	1.56%
11.4	0.93%	4.30%

The thrust and power are further examined using Case 2, i.e, specifying a surge motion for the turbine considered in Fig. 10. The surge motion is assumed to given as a sine function with an amplitude of 8 m and the circular frequency of 0.246 rad/s. The surge motion changes the relative velocity around the blades and cause the changes of the aerodynamic loads. A dynamic stall model for low Mach numbers developed from the Leishman–Beddoes (LB) semi-empirical model (Sheng et al., 2008; Leishman and Beddoes, 1989) is applied in this case to be consistent with results to be compared. The dimensionless thrust and power coefficients together with other numerical results in the cited references are plotted in Fig. 11 for one period of the surge motion. As can be seen from Fig. 11, the results from our new model are very close to the results from the high-fidelity simulation using the commercial software called Star-CCM+. The maximum relative difference is less than 10%.

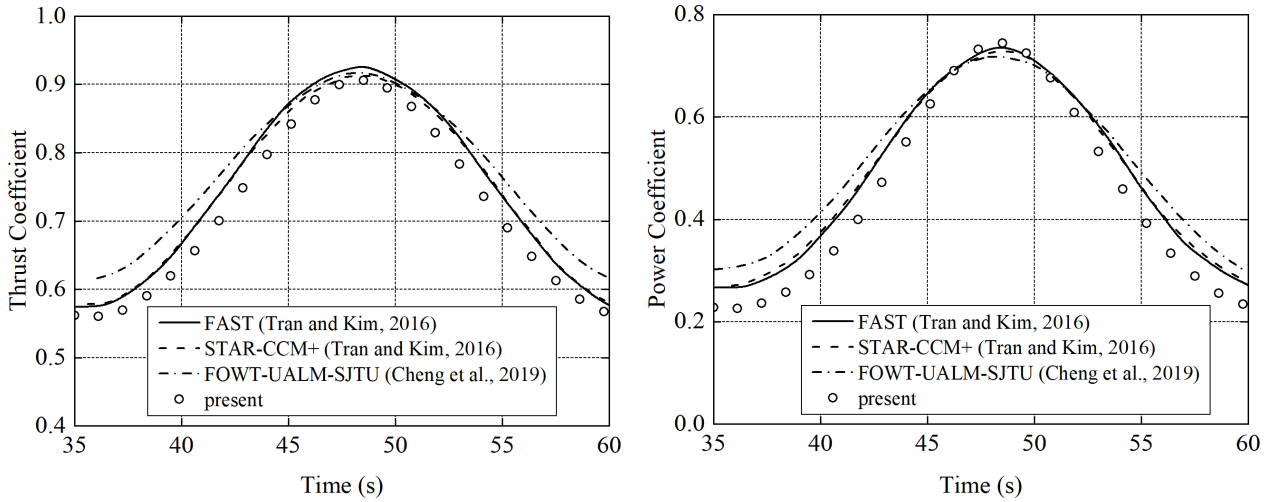

Fig. 11. Comparisons with different numerical results in literature for Case 2: (a) thrust coefficient; (b) power coefficient

The case for Fig. 11 is also simulated by using the traditional ALM without considering the deflection of blades and platform motions when estimating the aerodynamic loadings. This is to illustrates the effectiveness of the modified unsteady ALM introduced in this paper. A comparison of the thrust and power coefficients in the first two motion periods shown in Fig. 12. One can see that the results by the traditional ALM seems to be unreasonable while the present unsteady ALM can clearly capture the right phenomenon induced by the surge motion.

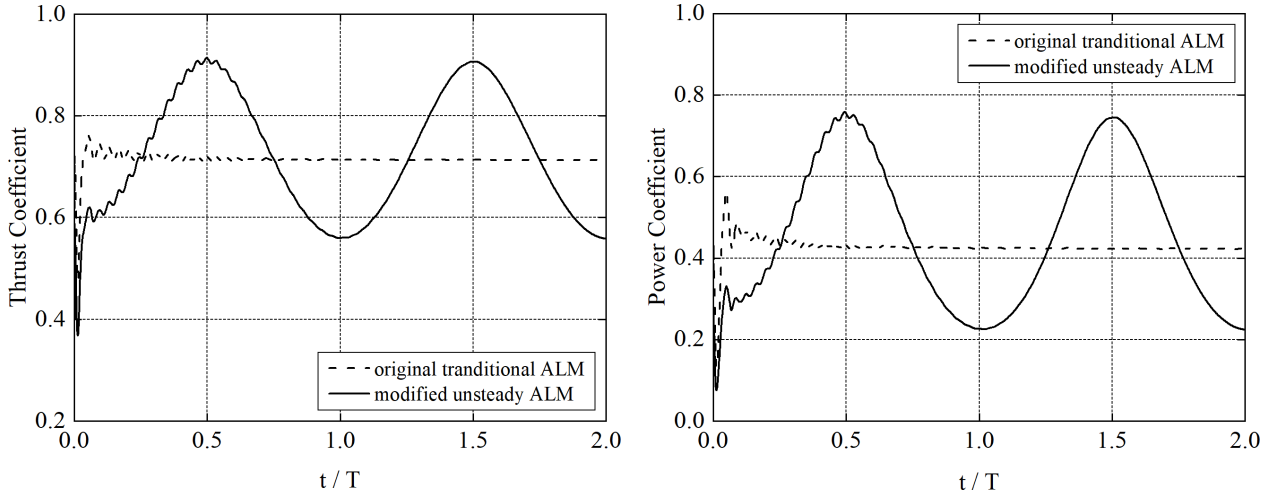

(a) (b)

Fig. 12. Comparisons of original and modified ALM results: (a) thrust coefficient; (b) power coefficient

4.2 Structural dynamics of a turbine blade

In this section, the blade structural dynamics will be first validated individually. For this purpose, only one blade (Fig. 13) of the turbine in the above cases will be examined. The blade is either fixed (Case 3) or rotated at a speed of 1.245 rad/s (Case 4). It undergoes a constant distribution load of 8000 N/m, applied at beginning of simulation. The flapwise blade tip displacements are presented in Fig. 14, together with the results obtained by FAST. It can be observed from Fig. 14 that the results of the two curves are almost identical. The amplitude of the blade vibration with a rotation in Fig. 14(b) is larger than that in Fig. 14(a) without rotation. Besides, the blade nature frequencies are also verified and summarized in Table. 4. It shows that the present model can accurately predict the 1st flap and 1st edge frequency. As the fluid dynamics are not considered in the cases, such good agreement between the results is expected.

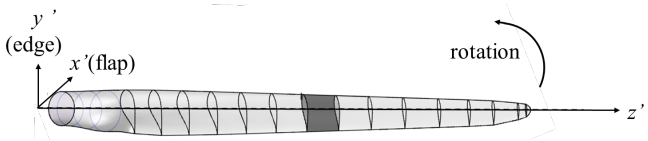

Fig. 13. Sketch of the blades together with its local coordinate system

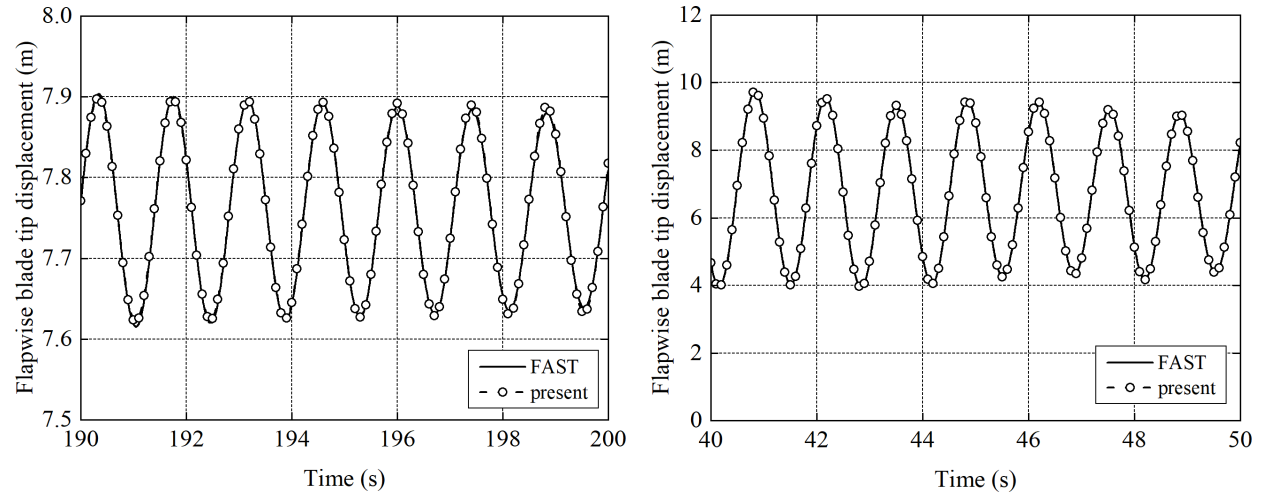

(a) (b)

Fig. 14. Comparisons of flapwise blade tip displacements: (a) fixed blade; (b) rotating blade

Table. 4 Comparison of the blade natural frequency with FAST results

Frequency point	Present (Hz)	FAST (Hz)	Error
Rotation	0.198	0.199	0.075%
Flap 1st	0.75	0.74	1.32%
Edge 1st	1.07	1.07	0.0%

Secondly, the flapwise blade displacement of the fixed wind turbine (Case 1) is also compared with the results from FAST in Fig. 15 to further examine if the new method can model the structure dynamics reasonably well under more complex conditions. Fig. 15 (a) gives the averaged displacement for different wind speeds while Fig. 15 (b) shows a time history in several periods of vibration at the rated wind speed (11.4 m/s). From this figure, one can see that the results with different wind speeds from different models are consistent with each other. Their relative differences in the averaged values are further detailed in Table. 5, showing the maximum relative difference is less than 3%. As seen from Fig. 15(b), the maximum amplitude of the vibration predicted by our new model is visibly larger than that from FAST. That is perhaps because the relative fluid velocity of the blade calculated by our CFD model is different from that of FAST that estimates the induced velocity using the momentum theory.

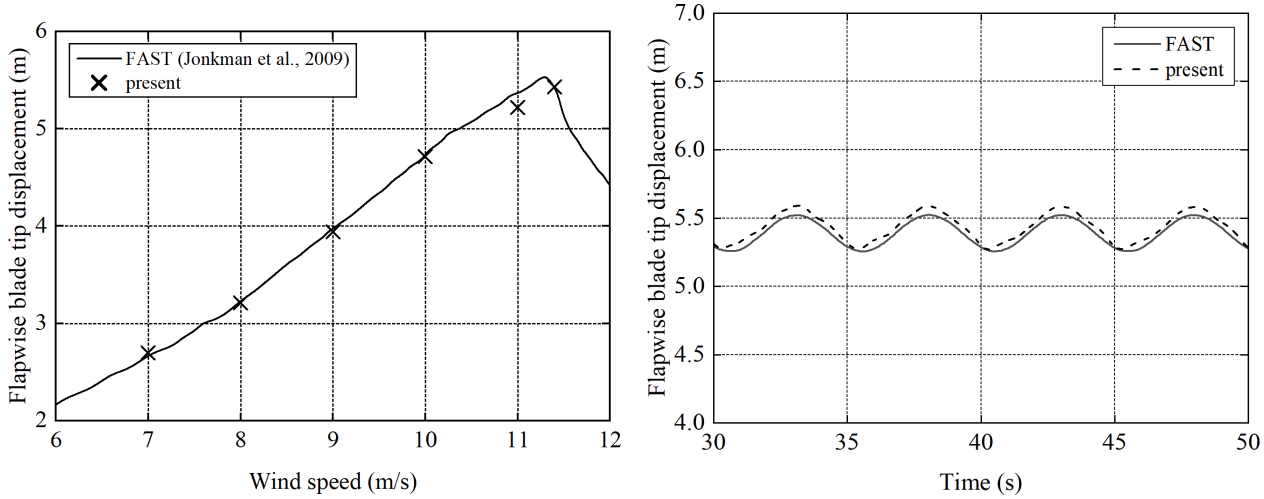

(a) (b)

Fig. 15. Comparison of the blade tip displacement results (a) averaged value with different wind speed; (b) time history with the rated wind speed

Table. 5 Relative differences of the averaged flapwise blade tip displacement with FAST results

Wind speed (m/s)	Differences
7.0	0.293%
8.0	1.084%
9.0	0.995%
10.0	2.704%
11.4	2.145%

3.3 Mooring dynamics and hydrodynamics of platform

One of important aspects for the qaleFOAM-BM is to couple the mooring dynamics with the platforms. This subsection will examine if this aspect works well. For this purpose, the cases (Case 5 and 6) for the sub-system of platform and mooring lines are considered (i.e., without the turbine, tower and wind). Case 5 examines the behaviors of the

subsystem at free decay tests while Case 6 examines surge, heave and pitch motions and the mooring tensions when the subsystem subjected to a regular wave. The numerical results will be compared with the experimental data from literature and those obtained by using another CFD software by other authors. Fig. 16 compares the damping ratios from the surge free decay test with different initial surge displacements while Fig. 17 shows the damping ratios from the heave free decay test with different initial heave displacements. One can see that the numerical results from the present method is in good agreement with the experimental data, and also with the numerical results from Tran and Kim (2015) in the most cases. Nevertheless, the difference between the damping ratio of surge obtained by present method and the reference at the initial displacement of 4 meters is quite large but our results seem to be closer to the experimental results. Fig. 18 (a) shows the time history of pitch motion for one initial displacement while Fig. 18 (b) shows the damping ratios for several pitch initial displacements. Again, the agreement between the results is very good. The natural periods obtained by the present method are compared with the experimental data (Coulling et al., 2013) in Table 6. The relative errors are less than 2.2% for the tests considered. Fig. 19 exhibits the tension at the fairlead of No.1 mooring line for different initial surge displacements. The predicted results in this paper are in excellent agreement with the experimental results.

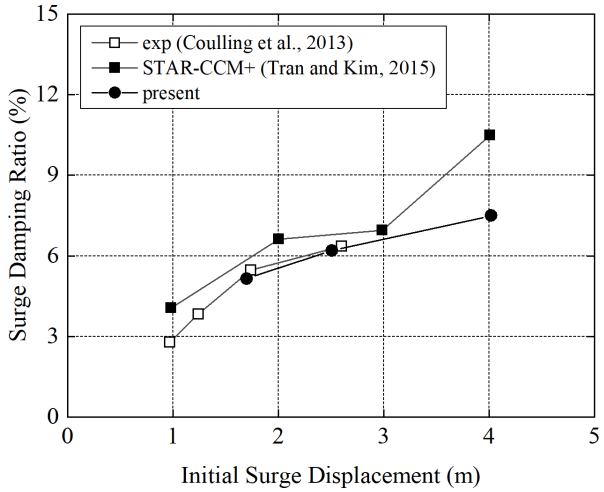

Fig. 16. Comparison of the damping ratios obtained by surge free decay tests with different initial surge displacements

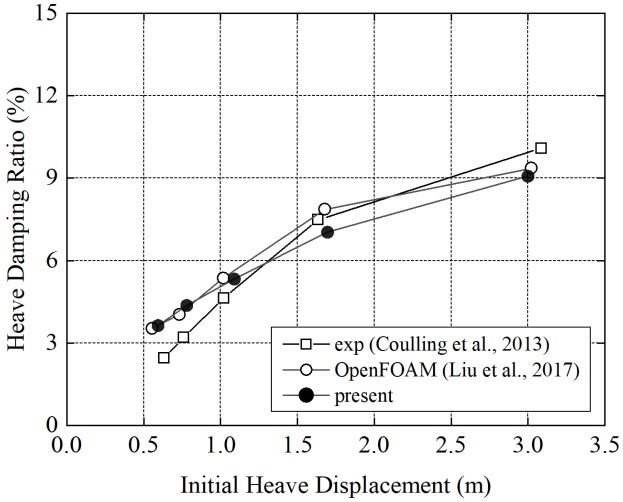

Fig. 17. Comparison of the damping ratios obtained by heave free decay tests with different initial heave displacements

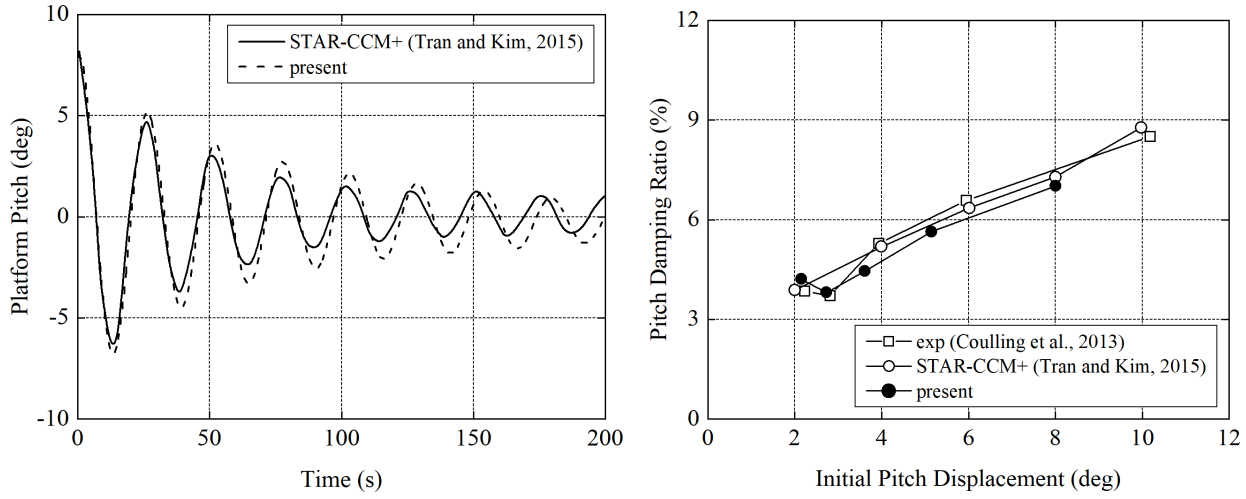

(a) (b)

Fig. 18. Comparison of pitch motion free decay test with initial pitch displacement: 8 deg: (a) time history for initial displacement of 8 deg; (b) damping ratios for different initial displacement

Table. 6 Comparison of natural periods with experimental data

DOF	Exp (s) (Coulling et al., 2013)	Present (s)	Error
Surge	107.0	109.3	2.14%
Heave	17.5	17.7	1.14%
Pitch	26.8	26.4	1.49%

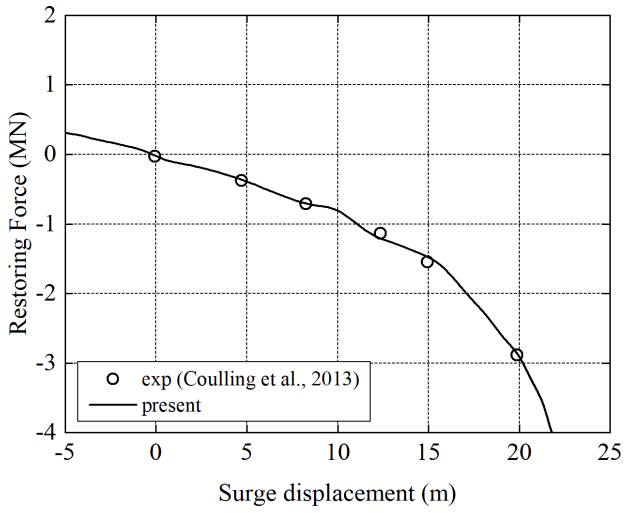

Fig. 19. Comparison of the mooring restoring force

When modelling Case 6, the sub-system is subjected to a regular head wave (along the direction of No. 1 mooring line) with a wave amplitude of 3.79 m and period of 12.1 s. The time histories of the surge and pitch are displayed in Fig. 20 while the Response Amplitude Operators (RAO) of surge, heave and pitch are compared in Fig, 21. The RAOs are calculated from the normalization of the motion amplitude by the amplitude of wave. The numerical results from present method agree very well with the experimental data and those obtained by other authors using different numerical models. All the results demonstrate that the newly developed method works well in various different situations.

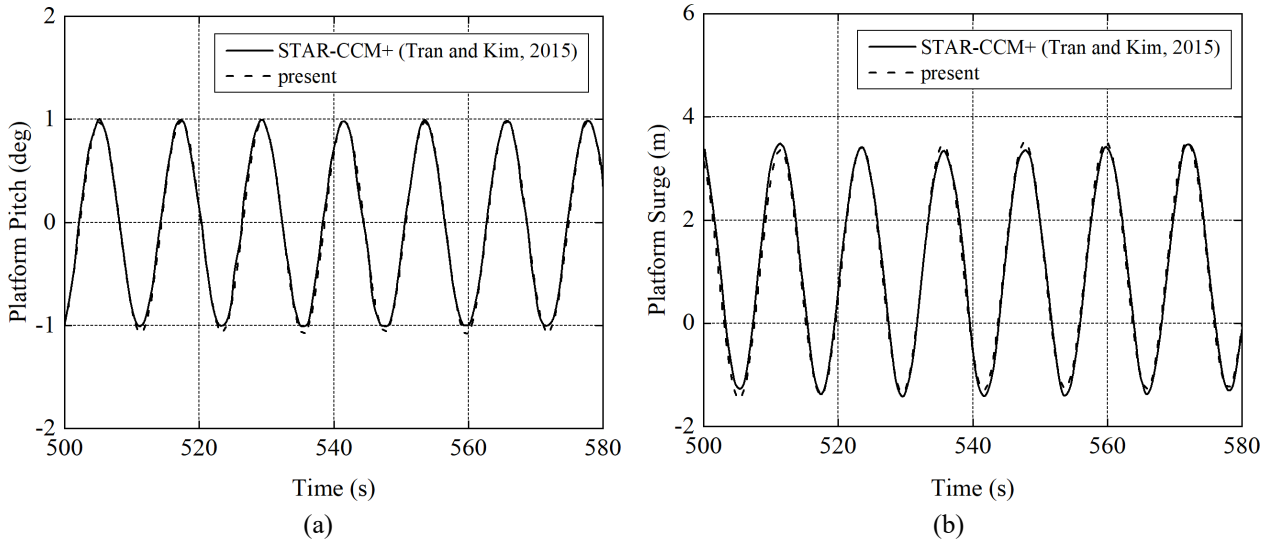

Fig. 20. Comparison of the platform motion response time history in regular wave: (a) pitch; (b) surge

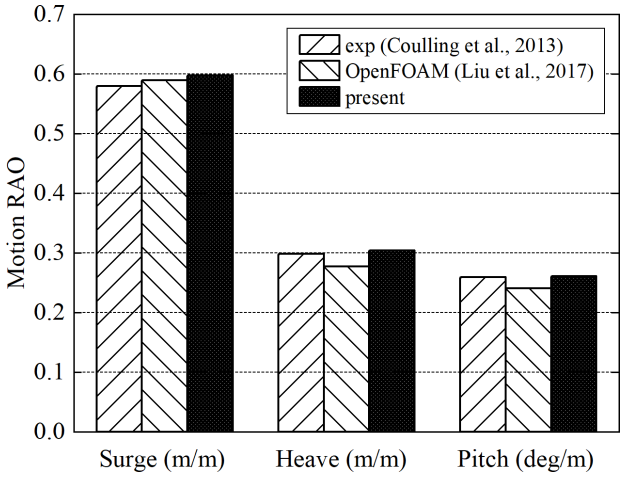

Fig. 21. Comparison of the platform Response Amplitude Operators (RAO) in regular wave

5. Simulation and Analysis of FOWT as whole system

On the basis of validation discussed above, the newly development method, qaleFOAM-BM, is applied to simulate the NREL 5 MW OC4 FOWT as a whole system consisting of three mooring lines, semi-submersible platform, tower/hub and three blades. In the simulation, the blades and mooring lines are allowed to undergo structure deflection and vibration while other parts are considered as rigid body. The domain size and other model details have been given in Section 3, including the incoming wind speed of 11.4 m/s with the direction normal to the rotational plan of the turbine, and the incoming regular wave with the height of 7.58 m and the wave period of 12.1 s in the direction along the No. 1 mooring line (shown in Fig. 7). The turbine rotates at a speed of 12.1 rpm (~0.2Hz). The results will be presented and discussed in several aspects.

5.1 Hydrodynamic responses

The time histories of the hydrodynamic responses in about one wave period after the responses become largely steady are plotted in Fig. 22, including the surge, heave and pitch motions of the system and the tension of No. 1 mooring lines. The corresponding oscillating amplitudes and the average values are summarized in Table. 7, which is estimated by using the time histories of 3 wave periods in the steady stage of the responses. The amplitude values are computed by the difference of the peak and the trough. For comparison, the case is also simulated by using the FAST code. The differences

between the results are presented in Table 7. The results show that the pitch, heave and surge motions by the two methods are similar to each other. Nevertheless, their amplitudes and mean values are visibly different with the relative difference of 4.44% to 11.30% (the near-zero average values of heave not given). These differences are likely to be caused by the fact that the FAST employs simple method to estimate the wave loadings on the platform, while these loadings are obtained by integrating pressure and shear stresses on the platform in the qaleFOAM-BM. The tension of No. 1 mooring line at fairlead is almost the same as that of FAST. The relative differences of both the mean and amplitude are less than 3%. That is perhaps because the mooring line model adopted in this paper is the same as that in FAST.

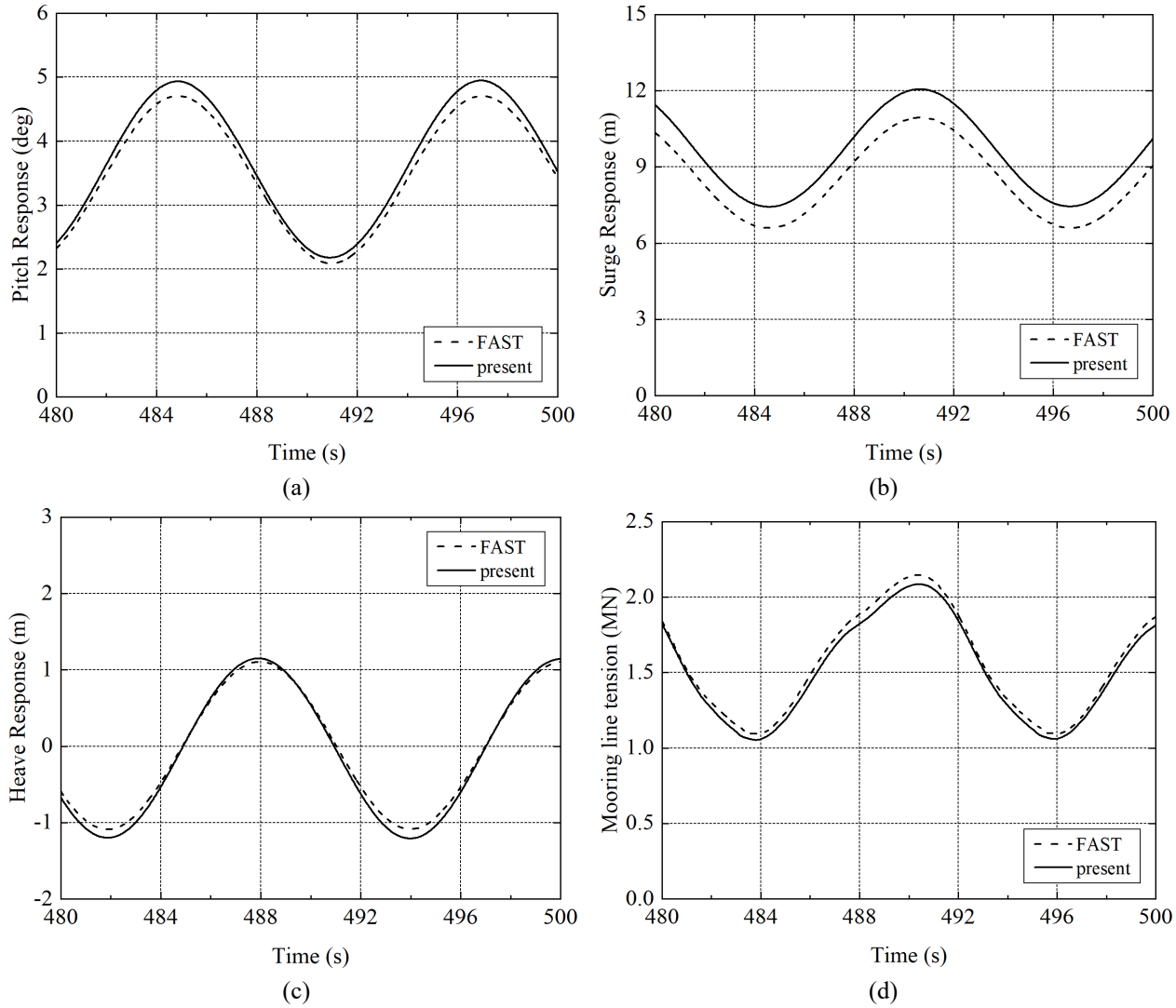

Fig. 22. Comparison of the hydrodynamic responses with FAST: (a) pitch motion; (b) surge motion; (c) heave motion; (d) tension of mooring line No. 1 at fairlead

Table. 7 Relative differences of the hydrodynamic responses with FAST

Dynamic responses		FAST	Present	difference
Pitch (deg)	Amplitude	2.616	2.786	6.50%
	Average	3.400	3.551	4.44%
Surge (m)	Amplitude	4.354	4.669	7.23%
	Average	8.773	9.764	11.30%

Heave (m)	Amplitude	2.194	2.336	6.47%
Mooring tension (MN)	Amplitude	1.051	1.038	1.21%
	Average	1.621	1.572	3.00%

5.2 Aerodynamic responses

The aerodynamic thrust and power of the turbine are compared in Fig. 23 and Table. 8. With the influence of platform motion, the thrust and power of the turbine oscillate at the same period (about 12.1s) as the incoming wave but with some negative pulses in between. The pulses occur when a blade passes the tower, called "tower shadow effect", caused by the disturbance of the tower to nearby flow field. Although the results obtained by the present numerical method are quite similar to those from FAST, the differences are clearly visible. The relative differences of average values are no more than 6% but the relative difference in the oscillating amplitude can reach more 12%.

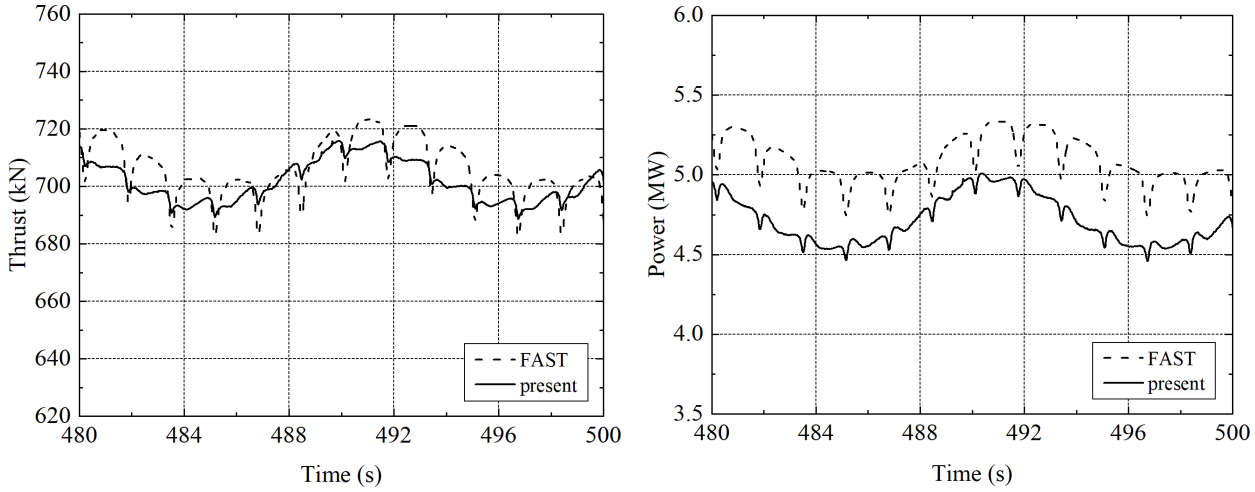

(a) (b)

Fig. 23. Comparison of the aerodynamic responses with FAST: (a) aerodynamic thrust; (b) power

Table. 8 Relative differences of the aerodynamic responses with FAST

Dynamic responses		FAST	Present	Differences
Thrust (kN)	Amplitude	40.4	27.46	-12.94
	Average	702.7	702.97	0.04%
Power (MW)	Amplitude	0.579	0.545	5.91%
	Average	5.043	4.749	5.82%

5.3 Blade dynamic responses

For the same case as in previous sections, the time histories of flapwise and edgewise blade tip displacements in about one wave period are shown in Fig. 24. It can be seen that the flapwise vibration is quite complex while the vibration in edge direction is quite regular. To further look at the causes behind the phenomenon related to the flapwise vibration, Fourier analysis is performed on it and the corresponding spectra are shown in Fig. 25. One can see several peaks in the spectra. Peak A corresponds to wave frequency, and peak C to turbine rotation frequency. Peaks B, D, E are attributed to the coupled effect between wind turbine rotation and platform motion. Peak F is caused by the ‘tower shadow effect’. Peak G corresponds to the natural frequency of flapwise, which is higher than the natural frequency without rotation. From the

results, it can be seen that the displacement in the flap direction of the blade tip is affected by the response of the FOWT, the wind turbine rotation, tower shadow effect and their interaction. The magnitudes of peaks, particularly at A, B, C, D and E from the present method are relatively smaller compared to those from FAST. Nevertheless, the differences between the frequencies obtained by the different methods are not significant as shown in Table. 9.

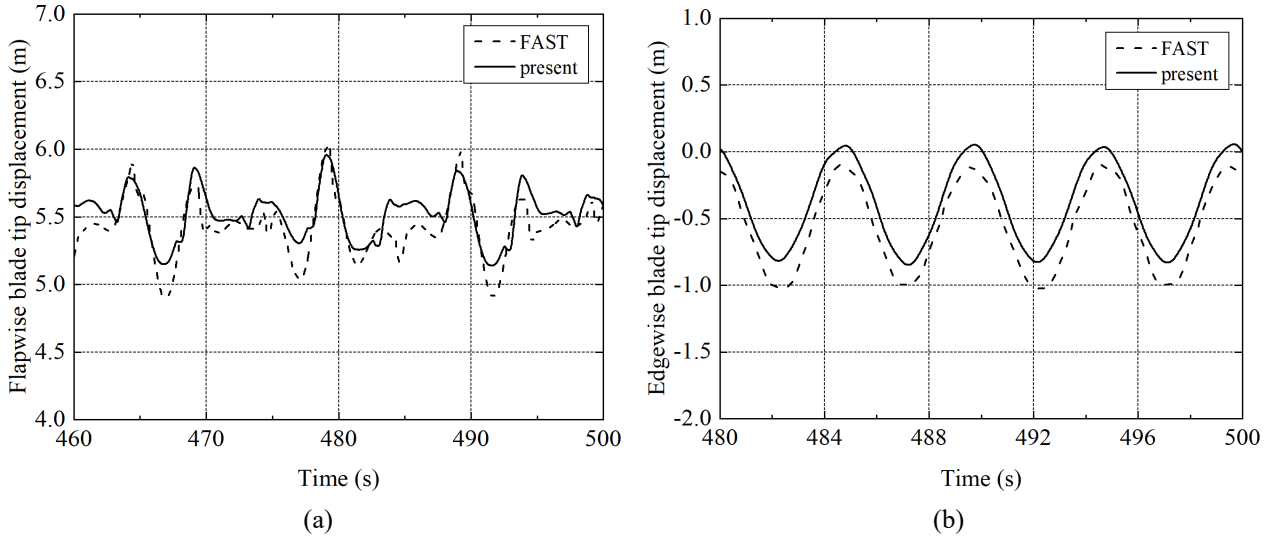

Fig. 24. Comparison of the aeroelastic responses with FAST: (a) flap; (b) edge

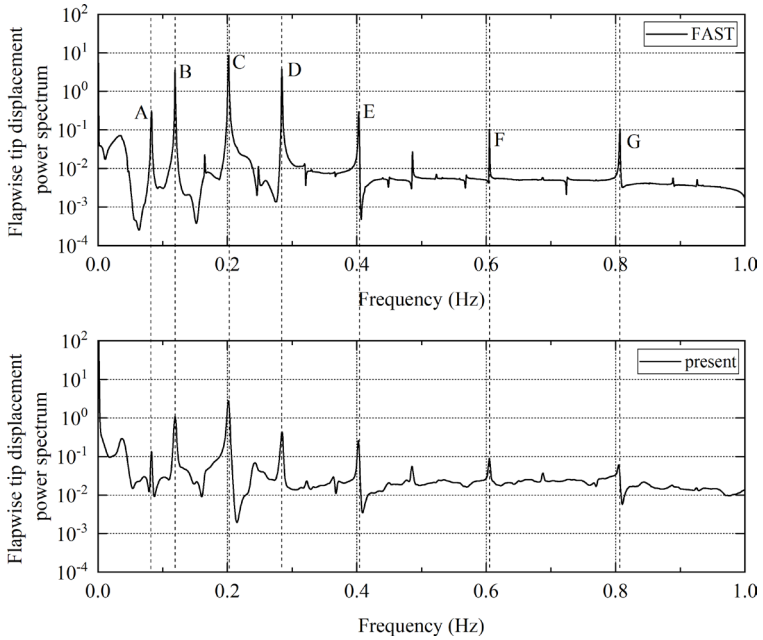

Fig. 25. Comparison of the Fourier analysis results of No. 1 blade flapwise tip displacement

Table. 9 Comparison of the frequency with FAST

Frequency point	FAST	present	differences
A	0.0829	0.0825	0.48%
B	0.1189	0.1200	0.93%
C	0.2009	0.2025	0.80%
D	0.2839	0.2850	0.39%
E	0.4029	0.4025	0.10%

F	0.6049	0.6050	0.02%
G	0.8059	0.8050	0.11%

5.4 Features of wake flow

The wake flow field, especially the interaction between FOWT and its wake, is examined. Fig. 26 describes the flow field of the FOWT in one incident wave period obtained by the present method. The vortex is visualized using the Q criterion, calculated by the second invariant of the velocity gradient tensor, and colored by the velocity magnitude. Firstly, the airflow near free surface is apparently affected by the wave propagation. Besides, the blade tip vorticities move through the wake flow behind wind turbine due to the motion of FOWT. It leads to the differences in the distance between adjacent vortexes at different time and thus disturbs the vortex structures. Moreover, the outline of the wake region boundary is not a smooth line but curved. Such phenomenon is not seen in case for a fixed turbine. It is caused by the FOWT motions. To quantify this influence, the time histories of the velocities at four positions behind wind turbine are compared in Fig. 27. One can see that the period of the curve is the same as the wave period (12.1 s). In addition, this influence becomes weaker with the increase in the distance of the points concerned.

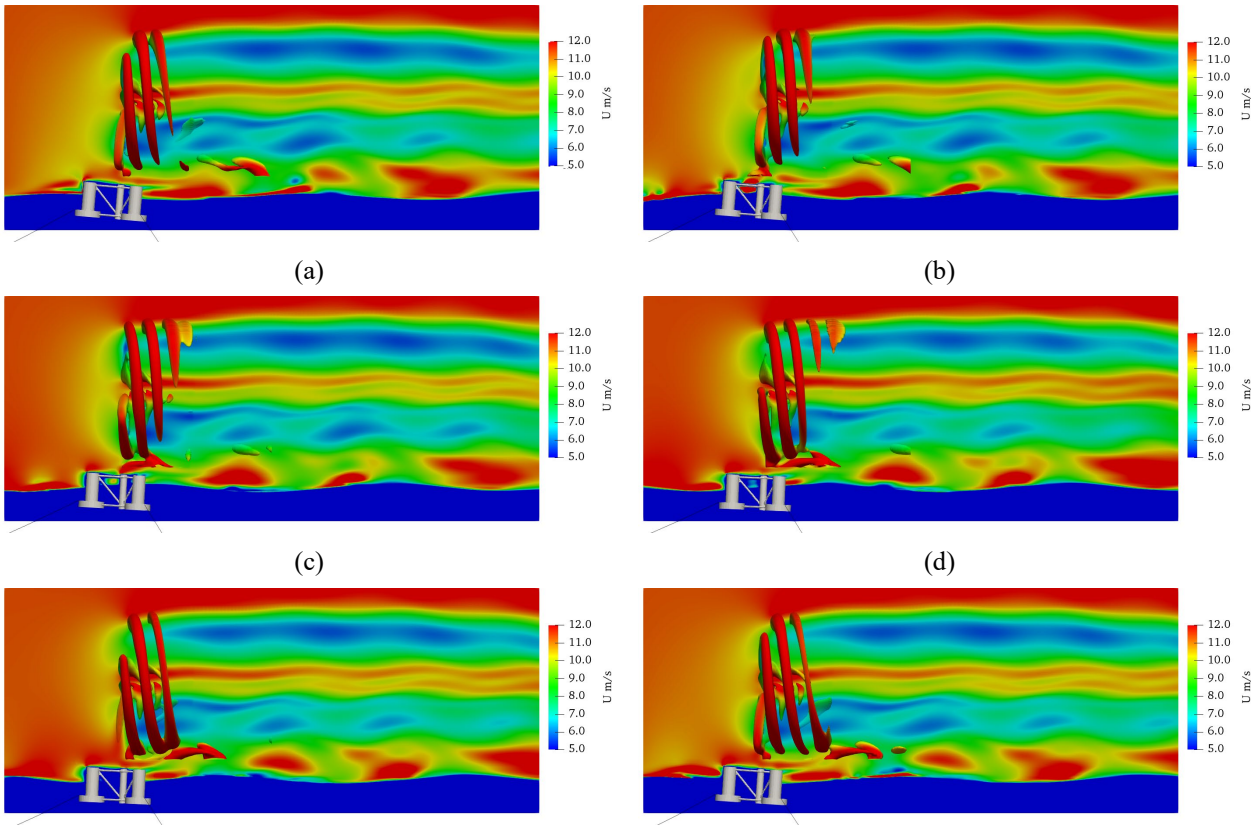

Fig. 26. Vortex near the wind turbine and flow field at midplane coloured by velocity: (a) 1/6 T; (b) 1/3 T; (c) 1/2 T; (d) 2/3 T; (e) 5/6 T; (f) T

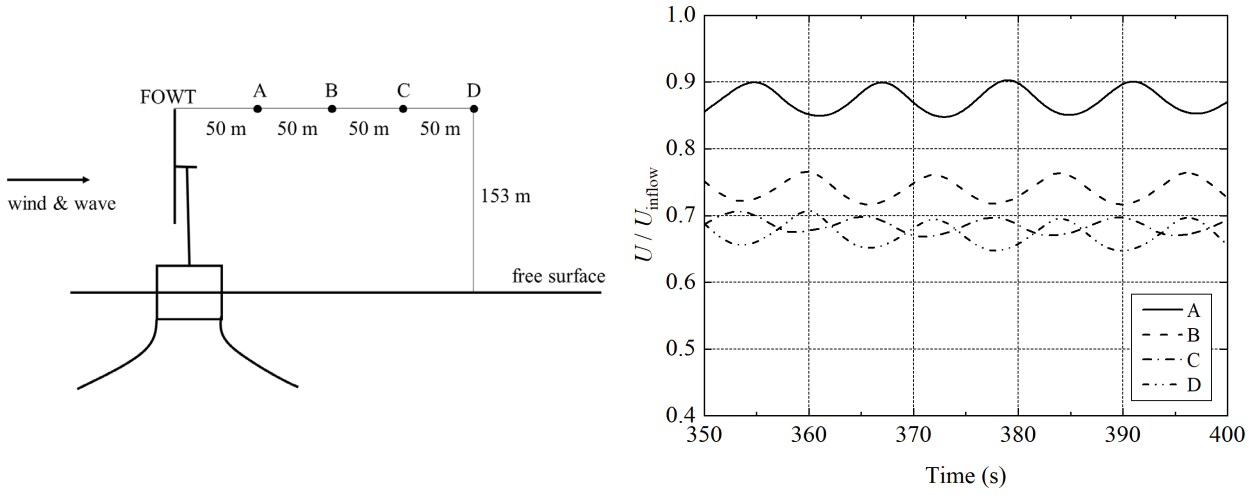

(a) (b)

Fig. 27. Time history of wind speed behind turbine rotor: (a) sampling point; (b) time history

5.5 Computational Efficiency

The method in this paper has adopted ALM to model the blades. It might be interesting to see how much the computational efficiency would be improved, relative to the case with the blades fully resolved in the fluid domain. For this purpose, we also simulate the same case corresponding to Sections 5.1-5.4 but with using the real shapes of blades, rather than using the ALM. The computational performance is measured by the speed-up ratio, equal to the computational time consumed by the case with the real blade shapes divided by the computational time with ALM. The result is compared in Fig. 28. As is observed, the computational efficiency of present model can be almost 3.5 times faster than that with using real blade shapes. It is noted that to avoid using too long time for the case with real blade shapes, the blades are considered rigid; otherwise the speed-up ratio would be much larger.

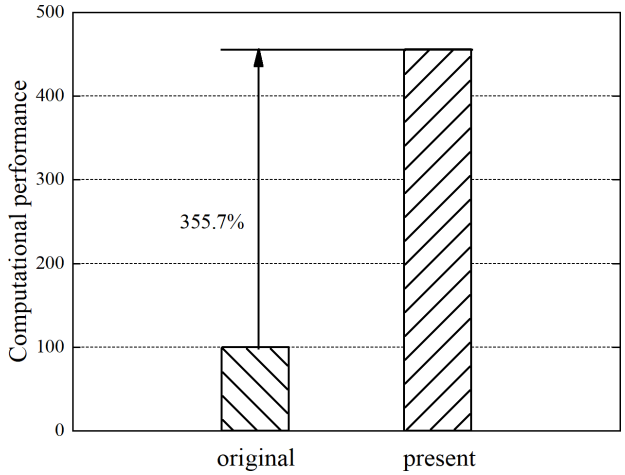

Fig. 28. Speed up ratio between present and original model

6. Conclusion

In this study, a new hybrid numerical model for FOWT systems is developed by combing the hybrid potential-viscous flow model (qaleFOAM) with the blade structural dynamic model (BeamDyn) and the mooring dynamics model (MoorDyn). In the new model, the aerodynamics of wind turbine blades, tower and hub are solved by an improved unsteady actuator line method (UALM); the structural responses of the turbine blades are simulated by the Legendre

spectral finite element model (BeamDyn); the mooring dynamics are considered with the Lumped Mass Mooring Model (MoorDyn), the fluid dynamics are dealt with by the combination of the fully nonlinear potential model with a two-phase Navier–Stokes model. The fully nonlinear potential model is run in a larger domain for generating and propagating the waves while the two-phase fluid dynamics is solved only in a region near the FOWT with the large eddy simulation (LES) modelling the turbulent effects. This newly formulated model can deal with wind, wave, mooring dynamics, platform motions, and turbine structural dynamics in a coupled way involved in the FOWT system.

The new numerical model is validated in various cases with different complexities by using the experimental data and other numerical results from literature. Generally speaking, the results from the new model have acceptable, sometime excellent, agreement with the results from the literature.

The present model is then applied to simulate the NREL 5 MW OC4 semi-submersible floating wind turbine as a whole system, which subjected to a regular wave and a rated wind speed. Different dynamics behaviors are examined, including the mean and dynamic aerodynamic loads of the wind turbine blades, the blade tip deflections, the hydrodynamic responses of the platforms and mooring tensions. All the results seem to reasonable. Nevertheless, more studies and validation on the model need to be carried out to further quantify its behaviors. In addition, the flexibility of tower will be considered in our future work.

Acknowledgement

The authors from Harbin Engineering would like to acknowledge the support of the National Natural Science Foundation of China (51739001, 51879051). The second author gratefully acknowledge the financial support of EPSRC, UK (EP/T00424X/1, EP/V040235/1)

References

Ahn H, Shin H. Experimental and Numerical Analysis of a 10 MW Floating offshore Wind Turbine in Regular Waves. energies, 2020, 13(10), 2608. https://doi.org/10.3390/en13102608

Bachant P, Goude A, Wosnik M. Actuator line modeling of vertical-axis turbines. arXiv: Fluid Dynamics, 2016. https://doi.org/10.48550/arXiv.1605.01449

Bruinsma N, Paulsen B T, and Jacobsen G. Validation and Application of a Fully Nonlinear Numerical Wave Tank for Simulating Floating Offshore Wind Turbines, Ocean Engineering, 2018, 147, 647--658. https://doi.org/10.1016/j.oceaneng.2017.09.054.

Carrión M, Steijl R, Woodgate M, Barakos G N, Munduate, X, Gomez-Iradi S. Aeroelastic analysis of wind turbines using a tightly coupled CFD-CSD method. Journal of Fluids and Structures, 2014, 50: 392-415. https://doi.org/10.1016/j.jfluidstructs.2014.06.029

Chen J H, Hu Z Q, Liu G L, Wan D C. Coupled aero-hydro-servo-elastic methods for floating wind turbines. Renewable Energy, 2019(130):139-153. https://doi.org/10.1016/j.renene.2018.06.060

Cheng P. Huang Y, Wan D. A numerical model for fully coupled aero-hydrodynamic analysis of floating offshore wind turbine. Ocean Engineering, 2019, 173: 183-196. https://doi.org/10.1016/j.oceaneng.2018.12.021

Coulling A J, Goupee A J, Robertson A N, Jonkman J M, Dagher H J. Validation of a FAST semi-submersible floating wind turbine numerical model with DeepCwind test data. Journal of Renewable and Sustainable Energy, 2013, 5. https://doi.org/10.1063/1.4796197

Duan X Z, Wang J H, Wan D C. CFD investigations of Wake Flow Interactions in a Wind Farm with 14 Wind Turbines. International Journal of Offshore and Polar Engineering, 2020, 30(3): 257-265. https://doi.org/10.17736/ijope.2020.mm23

Fleming P, Gebraad P M O, Lee S, van Wingerden J W, Johnson K, Churchfield M, Michalakes J, Spalart P, Moriarty P. Simulation comparison of wake mitigation control strategies for a two-turbine case. Wind Energy, 2015, 18: 2135-2143. https://doi.org/10.1002/we.1810

Hall M, Goupee A. Validation of a lumped-mass mooring line model with DeepCwind semi-submersible model test data. Ocean Engineering, 2015, 104: 590-603. https://doi.org/10.1016/j.oceaneng.2015.05.035

Hao H B, Guo Z Q, Ma Q W, Xu G C. Air cushion barge platform for offshore wind turbine and its stability at a large range of angle. Ocean Engineering, 2020, 217. https://doi.org/10.1016/j.oceaneng.2020.107886

Huang Y, Cheng P, Wan D C. Numerical Analysis of a Floating Offshore Wind Turbine by Coupled Aero-Hydrodynamic Simulation. Journal of Marine Science and Application, 2019, 4. https://doi.org/10.1007/s11804-019-00084-8

Jessen K, Laugesen K, Mortensen S M, Jensen J K, Soltani M N. Experimental Validation of Aero-Hydro-Servo-Elastic Models of a Scaled Floating Offshore Wind Turbine. applied sciences, 2019, 9(6), 1244. https://doi.org/10.3390/app9061244

Jonkman J, Butterfield S, Musial W, Scott G. Definition of a 5-MW Reference Wind Turbine for Offshore System Development. National Renewable Energy Laboratory, Golden, 2009, CO Technical Report No. NREL/TP-500–38060.

Leishman J G, Beddoes T S. A Semi-Empirical Model for Dynamic Stall. Journal of the American Helicopter Society, 1989, 34, 3-17. https://doi.org/10.4050/JAHS.34.3.3

Li Q, Wang J H, Yan S Q, Gong J Y, and Ma Q W. A Zonal Hybrid Approach Coupling FNPT with OpenFOAM for Modelling Wave-Structure Interactions with Action of Current, Ocean systems engineering, 2018, 8, 381--407. https://doi.org/10.12989/ose.2018.8.4.381.

Li Y, Castro A M, Sinokrot T, Prescott W, Carrica P M. Coupled multi-body dynamics and CFD for wind turbine simulation including explicit wind turbulence. Renewable Energy, 2015, 76: 338-361. https://doi.org/10.1016/j.renene.2014.11.014

Liu Y, Xiao Q. Incecil A. Peyrard C, Wan D. Establishing a fully coupled CFD analysis tool for floating offshore wind turbines. Renewable Energy, 2017, 112: 280-301. http://dx.doi.org/10.1016/j.renene.2017.04.052.

Liu Y C, Xiao Q, Incecik A, Peyrard C. Aeroelastic analysis of a floating offshore wind turbine in platform-induced surge motion using a fully coupled CFD-MBD method. Wind Energy, 2019a, 22: 1-20. https://doi.org/10.1002/we.2265

Liu Y C, Xiao Q. Development of a fully coupled aero-hydro-mooring-elastic tool for floating offshore wind turbines. Journal of Hydrodynamics, 2019b, 31(3): 1-13. https://doi.org/10.1007/s42241-019-0012-6

Ma, Q W, and Yan, S Q. Quasi ALE Finite Element Method for Nonlinear Water Waves, Journal of Computational Physics, 2006, 212(1), 52--72. http://dx.doi.org.10.1016/j.jcp.2005.06.014.

Ma, Q W, and Yan, S Q. QALE-FEM for Numerical Modelling of Nonlinear Interaction Between 3D Moored Floating Bodies and Steep Waves, International Journal for Numerical Methods in Engineering, 2009, 78, 713--756. https://doi.org/10.1002/nme.2505.

Reissner E. On one-dimensional large-displacement finite-strain beam theory. Studies in Applied Mathematics LII, 1973, 2: 87-95. https://doi.org/10.1002/sapm197352287

Shen W Z, Mikkelsen R, Sørensen J N, Bak C. Tip loss corrections for wind turbine computations. Wind Energy. 2005, 8(4):457-475. https://doi.org/10.1002/we.153

Sheng W, Galbraith R A M, Coton F N. A modified dynamic stall model for low Mach numbers. Journal of Solar Energy Engineering, 2008, 130. https://doi.org/10.1115/1.2931509

Shives M, Crawford C. Mesh and load distribution requirements for actuator line CFD simulations. Wind Energy, 2012, 16(8): 1183-1196. https://doi.org/10.1002/we.1546

Sørensen J N, Shen W Z. Numerical modeling of wind turbine wakes. Journal of fluids engineering, 2002, 124:393–399. https://doi.org/10.1115/1.1471361

Tran T T, Kim D H. The coupled dynamic response dynamic response computation for a semi-submersible platform of floating offshore wind turbine. Journal of Wind Energy and Industriall Aerodynamics, 2015, 147: 104-119. https://doi.org/10.1016/j.jweia.2015.09.016

Tran T T, Kim D H. Fully coupled aero-hydrodynamic analysis of a semi-submersible FOWT using a dynamic fluid body interaction approach. Renewable Energy, 2016, 92: 244-261. https://doi.org/10.1016/j.renene.2016.02.021.

Wang J X, Wang J H, Yan S Q, Ma Q W, Xia G H, An improved passive wave absorber for FNPT-NS solver, Proceedings of the 29th International Ocean and Polar Engineering Conference, ISOPE 2019. ISBN: 978-1-880653-85-2

Wang Q, Sprague M A, Jonkman J, Johnson N, Jonkman B. BeamDyn: A high-fideity wind turbine blade solver in the FAST modular framework. Wind Energy, 2016: 1-24. https://doi.org/10.1002/we.2101

Wang Q, Liao K P, Ma Q W. The Influence of Tilt Angle on the Aerodynamic Performance of a Wind Turbine, Applied sciences, 2020, 10, 5380. https://doi.org/10.3390/app10155380

Yan S Q, Ma Q W, Sriram V, Qian L, Ferrer P J M, Schlurmann T. Numerical and experimental studies of moving cylinder in uni-directional focusing waves. Proceedings of the 25th International Ocean and Polar Engineering Conference, ISOPE 2015, 711–718. ISBN: 978-1-880653-89-0

Yan S Q, Ma Q W, Wang J H, Zhou J, Self-adaptive wave absorbing technique for nonlinear shallow water waves, ASME 35th International Conference on Ocean, Offshore and Arctic Engineering, 2016. https://doi.org/10.1115/OMAE2016-54475

Yan, S, Wang, J, Wang, J, Ma, Q, and Xie, Z. CCP-WSI Blind Test Using qaleFOAM with an Improved Passive Wave Absorber, International Journal of Offshore and Polar Engineering, 2020, 30(01), 43--52. https//doi.org/10.17736/ijope.2020.jc781.

Yu Z Y, Yan S Q, Zheng X, Ma Q W, Hao H B. Numerical simulations of a floating offshore wind turbine in the focused wave with a hybrid model. Proceedings of the 31st International Ocean and Polar Engineering Conference, ISOPE 2021, 1453-1459. ISBN 978-1-880653-82-1

Yu Z Y, Yan S Q, Zheng X, Ma Q W, Hao H B. Numerical Simulation of a Floating Offshore Wind Turbine in Waves using qaleFoam. International Journal of Ocean and Polar Engineering. 2022, 32(1):39-48. https://doi.org/10.17736/ijope.2022.jc841

Yu Z Y, Zheng X, Ma Q W, Hao H B. Actuator Line Method for Simulating NREL 5-MW Turbine Wakes, Proceedings of the 28th International Ocean and Polar Engineering Conference, ISOPE 2018a, 401-406. ISBN 978-1-880653-87-6

Yu Z Y, Zheng X, Ma Q W. Study on Actuator Line Modeling of Two NREL 5-MW Wind Turbine Wakes, Applied Sciences, 2018b, 8(3), 434. https://dpi.org/10.3390/app8030434.

Yu Z Y, Hu Z H, Zheng X, Ma Q W, Hao H B. Aeroelastic Performance Analysis of Wind Turbine in the Wake with a New Elastic Actuator Line Model, Water, 2020, 12(5), 1233. https://doi.org/10.3390/w12051233.

Zhou Y, Xiao Q, Liu Y C, Incecik A, Peyrard C, Wan D C, Pan G, Li S W. Exploring inflow wind condition on floating offshore wind turbine aerodynamic characterisation and platform motion prediction using blade resolved CFD simulation. Renewable Energy, 2021, 182: 1060-1079. https://doi.org/10.1016/j.renene.2021.11.010